Lithium isotopes and partition coefficients in inorganic carbonates: proxy calibration for weathering reconstruction

Christopher C. Day[a,*], Philip A.E. Pogge von Strandmann[b,c], Andrew J. Mason[a]

[a] *Department of Earth Sciences, University of Oxford, South Parks Road, Oxford, OX1 3AN*
[b] *Institute of Geosciences, Johannes Gutenberg University, 55122 Mainz, Germany*
[c] *London Geochemistry and Isotope Centre (LOGIC), Institute of Earth and Planetary Sciences, University College London and Birkbeck, University of London, Gower Street, London, WC1E 6BS, UK*

Abstract

We report Li measurements from cave-analogue carbonate-precipitation experiments in order to: i) assess the expected isotope fractionation factors applicable to speleothem growth, and ii) contribute to the wider understanding of lithium incorporation in carbonates. The experimental setup closely mimics natural processes (e.g. precipitation driven by CO_2 degassing, low ionic strength solution, thin solution film) but within a laboratory setting that allows for controlled growth conditions (temperature, pCO_2, drip rate, carbonate saturation index and the composition of the initial solution). For the main batch of calcite growth experiments our average $1000\ln\alpha_{\text{calcite-solution}}$ is $-8.5 \pm 2(2\sigma)$. This low sensitivity of $1000\ln\alpha$ to in-cave growth conditions is encouraging for weathering intensity reconstruction using speleothem samples. At each temperature, growth rate was varied independently with calcite saturation indices ranging between 0.1 and 0.6, with no significant impact on either D(Li) or $1000\ln\alpha$. For the full range of growth conditions (considering all temperatures and calcite saturation indices) we observe a small but significant decrease in $1000\ln\alpha$, which we do not attribute to temperature. Based on an inter-study comparison we define LogDLi $= 0.09(\pm0.04) \times GR - 3.2(\pm0.2)$, where GR is growth rate in units of $10^{-8}\,\text{mmol}\,\text{cm}^{-2}\,\text{s}^{-1}$. This is similar to the previously defined relationship over a reduced range of growth rates. Over this study's full range of growth rates, $1000\ln\alpha = -0.13(\pm0.04) \times GR - 7.1(\pm0.3)$ is significant at the $\rho = 0.018$ level, consistent with a surface entrapment control. Future experiments should test factors such as growth rate and pH, independently of other variables, to further assess their role in defining $1000\ln\alpha$. A subset of 20 °C experiments, with increasing $[Mg]_{\text{solution}}$, provides $1000\ln\alpha$ for calcite, high-magnesian calcite (HMC) and aragonite. Our values of $1000\ln\alpha$ for these three mineralogies range between -7.3 and -10.7. For HMC and aragonite in particular there is close agreement with other published values of $1000\ln\alpha$ for $CaCO_3$ grown in laboratory and in natural settings. In agreement with measurements in bulk carbonates, benthic foraminifera and brachiopods, this suggests that differences in $1000\ln\alpha$ between carbonate mineralogies may not always be as large as suggested by some earlier studies.

Keywords: inorganic calcite lithium partitioning, lithium isotopes, speleothem, weathering intensity, localised weathering, lithium partition coefficient, cave-analogue experiments, stalagmite

*Corresponding author
Email address: chris.day@earth.ox.ac.uk (Christopher C. Day)

1. Introduction

The terrestrial chemical weathering of silicates is a fundamental component of the global cycle of carbon and other elements. This is because during silicate weathering, atmospheric carbon is dissolved (as alkalinity), combined with cations such as Ca and Mg from rock dissolution, and transported to the oceans where the carbon is ultimately precipitated as carbonate and eventually buried (Walker et al., 1981; Berner et al., 1983). This means that silicate weathering exerts a strong control on the CO_2 concentration of the atmosphere, and hence global climate. Controls on the rate and style of weathering include temperature, rainfall/runoff and the supply of fresh silicate material (West et al., 2005), but separating the relative importance of these controls over geological time has been challenging, meaning that it is difficult to discern the primary controls over long timescales (Archer et al., 2000; Foster and Vance, 2006).

Li isotope ratios in marine proxy archives (e.g. Hathorne and James, 2006; Misra and Froelich, 2012; Pogge von Strandmann et al., 2013) and other proxies of past weathering from the marine environment, including Be (e.g. Von Blanckenburg et al., 2015), radiogenic Sr (e.g. Mokadem et al., 2015), Pb-isotopes (e.g. Crocket et al., 2013; Bailey et al., 2013) and Hf-Nd isotopes (e.g. Bayon et al., 2009; Vervoort et al., 2011), are fundamental in facilitating long-term reconstruction of weathering inputs to the ocean (e.g. alkalinity, nutrients), which in turn impact on the atmospheric (e.g. CO_2 concentrations) and terrestrial systems (e.g. ice volume, rainfall patterns, vegetation distribution).

Li isotopes in river waters (e.g. Huh et al., 1998; Vigier et al., 2009; Kisakurek et al., 2005; Dellinger et al., 2015) provide valuable insight into the modern-day weathering system at catchment or regional levels, but, unlike sedimentary records, $\delta^7Li_{solution}$ (i.e. the lithium isotopic ratio in solution expressed relative to a standard such as LSVEC) is applicable mainly to discrete measurement points in the modern, without the scope to extend that record back in time.

Changes in past seawater δ^7Li are thought to be recorded in marine carbonates (Dellinger et al., 2018), and have been used to reconstruct past weathering (Hathorne and James, 2006; Misra and Froelich, 2012; Pogge von Strandmann et al., 2013). However, the marine residence time of Li is long ($\sim$ 1 Myr), which impedes the use of δ^7Li measured in marine carbonates for reconstructing weathering changes on timescales shorter than hundreds of kyr. Hence, the ability to assess weathering for particular (i.e. local-scale) environments from local continental records, and at timescales less than the seawater residence time (including in the modern climate system), would be a powerful addition to the range of tools used to assess weathering.

In recent decades, speleothems (secondary calcium carbonate deposits in caves) are being shown to provide exceptional records of terrestrial and atmospheric environmental parameters in karst environments. Speleothems allow, for example, the reconstruction of rainfall isotopic values (e.g. Hendy, 1971; Mattey et al., 2008; Carolin et al., 2013), relative rainfall amounts (e.g. Fairchild et al., 2000), absolute rainfall amounts (e.g. Hu et al., 2008; Owen et al., 2016), vegetation/soil characteristics (e.g. Dorale, 1998; Genty et al., 2003), and there are increasing efforts to enable temperature reconstruction (e.g. Affek et al., 2008; Krüger et al., 2011; Kluge et al., 2015). This is possible because speleothems act as recorders of water composition at various points along the flow path between the surface and the water table (Fig. 1). Dissolution of silicates (e.g. allochthonous dust) within rivers and/or the soil zone (rich in CO_2, organic acids and bacteria) and subsequent precipitation of secondary minerals (e.g. clays) controls the lithium isotope ratio in solution, with this balance between dissolution and precipitation referred to as 'weathering congruency'. This weathering-controlled solution composition is recorded in speleothem carbonate material as it precipitates from solution.

Lithium is enriched in silicates by a factor of $\sim 10^2$ to 10^4 relative to crustal carbonates (Hathorne and James, 2006; Pogge von Strandmann et al., 2013; Gou et al., 2017; Pogge von Strandmann et al., 2017), so that, even in carbonate catchments, the predominant Li isotopic signal is from the weathering of silicate rocks (Kisakurek et al., 2005; Millot et al., 2010). Pogge von Strandmann et al. (2017) have successfully demonstrated speleothem recording of weathering congruency over glacial-interglacial timescales from Soreq and Tzavoa caves in Israel. This work promises significant progress in our ability to investigate weathering controls at a much higher spatial and temporal resolution. But this requires a robust understanding of the controls on lithium isotope incorporation from the solution into the solid in speleothem growth conditions. We need to understand whether factors such as temperature or growth rate will affect lithium isotopes in speleothems, thereby altering the weathering signal. Whilst there are some measurements of modern $\delta^7Li_{calcite}$ and $\delta^7Li_{solution}$ from Soreq cave (Pogge von Strandmann et al., 2017), these apply only to the modern day temperature of $\sim 20\,^{\circ}C$ and are insufficient for investigating controls on lithium isotope fractionation factors applicable to caves. There are two other sources of $1000 \ln \alpha_{calcite\text{-}water}$ for inorganic calcite (Marriott et al., 2004a,b), but with significant differences in the fractionation factors that they report (-8.5 and -3 respectively), and with growth conditions that are significantly different from those applicable to caves (i.e. with thin-film, low ionic-strength solutions and fast CO_2 degassing). The aim of this study was to grow calcite material according to the the natural mechanisms of calcite precipitation in caves, where calcite

supersaturation is reached by CO_2 degassing from a thin film solution, rather than from simple mixing of $CaCl_2$ and $NaHCO_3$. We start with a range of different temperatures, to ensure relevance of our results to a wide coverage of terrestrial sites. At each temperature we test for the influence of growth rate, over as large a range of growth rates as we believe possible, without inducing uncontrolled spontaneous precipitation. We were keen to compare our growth rates with those from natural settings to test for the applicability of our results. And we aim compare our results with former studies from calcite forming in different settings, to contribute to a wider understanding of lithium incorporation into carbonates.

2. Methods

2.1. Cave-analogue experimental setup

Complete details of the experimental setup are provided in Day and Henderson (2011, 2013). Here we provide a brief overview, and focus on the details that relate specifically to this study of lithium in inorganic calcite.

The setup closely mimics inorganic stalagmite formation (e.g. precipitation driven by CO_2 degassing, low ionic strength solution, thin solution film) but with a tight control on growth conditions (temperature, pCO_2, drip rate, calcite saturation index and the composition of the initial solution). We use two reaction vessels, one with high pCO_2 (20 000 ppmv, the 'dissolution chamber') and one with low pCO_2 ($<$1500 ppmv, the 'precipitation chamber'). Solution from the dissolution chamber, with a controlled calcite saturation index ($SI_{calcite}$), is pumped, by peristaltic pump, to drip onto a lightly frosted glass plate in the precipitation chamber, where CO_2 degassing from solution drives calcite growth. Experiments were performed at 7 °C, 15 °C, 25 °C and 35 °C. At each temperature, experiments were conducted simultaneously at two different calcite saturation indices, 'low' and 'high' to induce slower and faster growth respectively, with these saturation indices detailed below and in table 1. Starting solutions in the dissolution chamber are made to specific calcite saturation indices (reported in table 3) by using PHREEQC to calculate the mass of dissolved calcite required to produce our chosen calcite saturation index for a given solution volume, temperature and dissolution-chamber pCO_2 (20 000 ppmv in all cases). The calcite dissolution procedure and subsequent equilibration to a headspace pCO_2 value of 20 000 ppmv are described in detail in section 2.1 of Day and Henderson (2011). Prior to the experiments, 715 µg of calcite seed was grown on the 7 °C glass

plates to help initiate growth in these slow growth conditions. This seed was grown by allowing 15 x 10 µL drops of growth solution to fully evaporate from these two plates (at 7 °C).

To cater for the low partitioning of Li into calcite: i) we increased growth mass with longer experiments (21 days instead of 7); ii) we selected the solution flow rate (0.69 ± 0.10 mL min^{-1}) that was shown to maximise calcite precipitation in these conditions (Day and Henderson, 2011); and iii) $[Li]_{solution}$ was increased from $\sim 3 \times 10^{-6}$ mol L^{-1} (applicable to Day and Henderson, 2011, 2013) to $\sim 5 \times 10^{-5}$ mol L^{-1} (table 1). The low $SI_{calcite}$ was increased from 0.1 to 0.2 for the lower temperature experiments (7 °C and 15 °C) to increase growth mass. The high $SI_{calcite}$ was reduced from 0.6 to 0.5 for the high temperature experiments (25 °C and 35 °C) to reduce the risk of spontaneous precipitation in the initial solution. In all cases we have a significant difference in growth rate at each temperature to assess the effect of growth rate on lithium incorporation. For full details of the solution compositions c.f. table 1.

2.2. Lithium isotope chemistry and analyses

These pure experimental carbonates were dissolved in metal-free clean laboratories at room temperature in 1M HCl. Sufficient mass was dissolved to obtain 9 ng Li, necessary for both Li isotope and Li/Ca analyses (on the order of 2.6 mg $CaCO_3$). The Li isotope purification chemistry for carbonates has been described in several publications (Pogge von Strandmann et al., 2013, 2017). Briefly, a two-column procedure was used, both containing the cation exchange resin AG50W-X12. The first column contained ~2.4 mL resin and the second 0.5 mL resin, and Li was eluted in dilute HCl. Given that Li isotopes are fractionated during ion chromatography, yields were tested by collecting splits before and after the Li collection bracket. Results showed that <0.1% of Li was present in these splits, suggesting that close to 100% was in the fraction collected for analysis. Most analyses were performed on a Nu Plasma HR multi-collector inductively coupled plasma mass spectrometer (MC-ICP-MS) at the University of Oxford, using a sample-standard bracketing system relative to the LSVEC standard. The final sample set were analysed using a Nu Plasma 3 MC-ICP-MS at University College London (UCL), relative to the IRMM-016 standard. LSVEC measured relative to IRMM-016 on this machine yields $\delta^7Li = -0.003 \pm 0.054$‰ (2se, n=19), in keeping with other studies (Jeffcoate et al., 2004; Phan et al., 2016; Pogge von Strandmann et al., 2019a). Background instrumental Li intensities (typically 3 mV to 7 mV), measured in clean acid, were subtracted from both standard and sample intensities (typically 2 V in Oxford, and 10 V at UCL). The total procedural blanks were generally

indistinguishable from background, and contained ∼0.02 ng to 0.05 ng Li at Oxford, and <0.003 ng Li at UCL (Pogge von Strandmann et al., 2019a). All reported δ^7Li values have been re-normalised to LSVEC, and the reported uncertainty has been compounded to encompass analytical uncertainty on both samples. Accuracy and external reproducibility were assessed in both laboratories using seawater and the USGS standard BCR-2. In Oxford, these yielded $\delta^7\text{Li} = 31.3 \pm 0.6$‰ ($2\sigma$, n = 59, chemistry = 59, where "chemistry" denotes separate passes through full purification chemistry) for seawater, and 2.7 ± 0.4‰ (n = 4, chemistry = 4) for BCR-2. At UCL, seawater is $\delta^7\text{Li} = 31.1 \pm 0.4$‰ (n = 12, chemistry = 12) and BCR-2 has $\delta^7\text{Li} = 2.6 \pm 0.3$‰ (n=5, chemistry = 3). These values are all within uncertainty of previously published data (Dellinger et al., 2015; James and Palmer, 2000; Jeffcoate et al., 2004; Liu et al., 2013; Pogge von Strandmann et al., 2011; Pogge von Strandmann and Henderson, 2015).

2.3. Li/Ca analyses

Growth solutions and dissolved sample carbonates were measured for their trace-element composition using a PerkinElmer NexIon 350D quadrupole ICP-MS with a universal cell (collision, reaction or standard modes of operation) at the University of Oxford, Department of Earth Sciences. All measurements were made with the cell operating in collision mode, with He used as the cell gas. The minor calcium isotope ^{43}Ca was selected to ensure that all elements reported here are measured in pulse mode, with fewer than 2×10^6 counts per second. Minor/trace element-to-Ca ratios were determined for Li, Mg, Co, Sr, Cd and Ba using the 'ratio' method of Y Rosenthal et al. (1999). External precision (final row of table 1) was quantified using a secondary quality control standard produced by CPAchem Ltd, interspersed repeatedly during sample analysis, and is reported as 2x the relative standard deviation (RSD) on all analyses. As a check on accuracy, all of the quality control measurements were in agreement with the values reported by CPAchem Ltd, within the analytical uncertainty reported in table 1. Additional indicators of the combined reliability of the measurements and of the experimental setup preparation include: i) $[\text{Ca}]_{\text{solution}}$ values are within 1% of what is expected from the mass values of Ca and H_2O used to prepare the solutions, ii) $\text{Li/Ca}_{\text{solution}}$ values are within 13% of the target value of 1.5×10^{-2} mol mol^{-1}.

2.4. Crystallography and X-Ray Diffractometer (XRD) measurements

The crystal growth method used in these cave-analogue experiments is the same as the one employed in the former Day and Henderson (2011, 2013) calcite-growing cave-analogue experiments. An exception

to this is a separate subset of experiments at 20 °C, to investigate the effect of $[Mg]_{solution}$ on Li isotope fractionation.

Crystallography was assessed with optical microscopy for all experiments, with many areas of each plate assessed, particularly within the small section of the 'splash zone' area of the plate from which samples were taken for Li-isotope analysis. XRD analyses were conducted specifically for the 20 °C experiments, a separate subset of experiments with varying $[Mg]_{solution}$. Additional XRD measurements were conducted for growth material material at 7 °C, 25 °C and 35 °C, as specified in table 5. The carbonate samples used for the XRD-checks were recovered post XRD-analysis to be used for Li-isotope analysis. This ensures that we have XRD results relating directly to Li-isotope measurements.

X-ray diffraction was performed on sample powders/crystals scraped from the frosted glass plate growth substrate. Samples were mixed with anhydrous ethanol and deposited on a zero-background single crystal silicon substrate; samples were analysed using a PANalytical Empyrean Series 2 diffractometer operating at 40 kV and 40 mA with a Co Ka source. Samples were analysed in reflection-transmission mode while continuously rotated, and data were acquired from 5° to 85° 2theta using a step size of 0.026° which took approximately 20 minutes per sample. Diffraction data were reduced using the HighScore Plus software suite, and mineral identifications were based on the correspondence of d-spacings, intensities and profiles to the International Centre for Diffraction Data Powder Diffraction File 4+ database and quantified through the reference intensity ratio method (Snyder and Bish, 1989).

2.5. Seed correction for $\delta^7 Li_{calcite}$ measurements at 7 °C

Prior to the 7 °C experiments, small masses (0.7 mg) of seed calcite were grown on these low temperature glass plates to help initiate growth in these slow growth conditions. This compares with 7.4 mg and 28.5 mg of sample growth for the 7 °C experiments. This seed was grown by allowing 15×10 µL drops of growth solution to fully evaporate from these two plates (at 7 °C). To correct for the lithium contributed by the seed material to the 7 °C experiments, we use the lithium partition coefficient D(Li). The partition coefficient D(Li) used here and elsewhere in the document is defined as $D(Li) = \frac{(Li/Ca)_S}{(Li/Ca)_L}$, where $(Li/Ca)_S$ is the molar ratio of Li to Ca in the solid and $(Li/Ca)_L$ is the molar ratio of Li to Ca in the liquid (McIntire, 1963). We use D(Li) at 7 °C, extrapolated from the relationship between D(Li) and temperature defined by the 15 °C, 25 °C and 35 °C experiments (Fig. 3) to establish the number of moles of Li in the sample ($[Li]_{smp}$). We apply

this to the isotope mass balance equation $\delta^7\mathrm{Li}_{\mathrm{smp}} = \frac{\delta^7\mathrm{Li}_{\mathrm{mix}} \times [\mathrm{Li}]_{\mathrm{mix}} - \delta^7\mathrm{Li}_{\mathrm{seed}} \times [\mathrm{Li}]_{\mathrm{seed}}}{[\mathrm{Li}]_{\mathrm{smp}}}$. The number of moles of Li in the seed is $[\mathrm{Li}]_{\mathrm{seed}} = [\mathrm{Li}]_{\mathrm{mix}} - [\mathrm{Li}]_{\mathrm{smp}}$. $[\mathrm{Li}]_{\mathrm{mix}}$ and $\delta^7\mathrm{Li}_{\mathrm{mix}}$ were measured by mass spectrometry. The lithium isotopic ratio of the seed, $\delta^7\mathrm{Li}_{\mathrm{seed}}$, is equal to the measured value of $\delta^7\mathrm{Li}_{\mathrm{solution}}$ because the seed was grown by fully evaporating the solution. This results in the slow and fast growth rate 7 °C experiments being corrected from −6.7‰ to −7.8‰ and from −5.6‰ to −6.5‰ respectively.

These results were checked against a third 7 °C experiment, seeded in the same way, with a growth mass of 83.7 mg (due to a longer 128 second drip interval). The proportion of seed in that case was only 0.8% of the sample mass. Without correcting the isotopic measurement of that third experiment for seed we obtain $1000 \ln \alpha = -7.9$, which is in good agreement with our two seed-corrected samples (-7.8 and -6.5).

2.6. Average surface area normalised growth rate

We use the whole plate calcite growth mass combined with the experiment duration and the crystal surface area across the whole plate to establish an average surface area normalised growth rate. To produce estimates of the calcite surface area available for the nucleation of calcite precipitation, we develop a method (described below) that uses digital images of in-situ crystals. The image-processing package ImageJ (Rasband, 2012) is used for image analysis. This image-based approach was taken because of insufficient quantities of calcite growth in these cave-analogue conditions for surface area analysis using the Brunauer-Emmette-Teller (BET) approach and theory. We only apply this method to the calcite mineralogy because of the sufficiently simple rhomboidal shape of calcite crystals. The high-magnesian calcite and aragonite growth rates are only reported in units of $\mu\mathrm{g\,h}^{-1}$ (table 3).

At the end of each experiment, the plate and sample growth is photographed (step 1). We do so in cross-polarised light to emphasise crystal growth relative to the dark glass background (Fig. 6A). To cater for heterogeneous calcite growth across the plate we define up to three levels of calcite coverage (low, high and complete) for each experiment/plate (step 2). Complete calcite coverage applies to parts of the faster growth experiments in which the plate is completely covered with calcite crystals, as verified with microscopy. We use the thresholding function of ImageJ on a greyscale version of the image to establish the percentages of the plate representing low, high and complete calcite-coverage areas. Here, thresholding involves selecting a range of greyscale values (between 0 and 255) that represents a given level of calcite coverage of the plate. The pixels fitting within the selected range of greyscale values are coloured red by ImageJ and the percentage

of the image fitting that threshold is given. These percentage values are multiplied by the surface area of the plate (46.8 cm^2) to give the surface area of the low, high and complete calcite-coverage areas. In Fig. 6B, the high calcite-coverage areas, represented by the threshold range 0 to 140, are coloured red and occupy 46% (21.5 cm^2) of the plate area. In Fig. 6C, the low calcite-coverage areas are coloured red, they occupy 54% (25.3 cm^2) of the total plate area and correspond to the threshold range 141 to 255.

Step 3 establishes the average two-dimensional surface area of calcite crystals within the low, high calcite-coverage areas. This is done with 2-3 microscopy images representative of each area. Any type of microscope image is suitable, providing that there is a sufficiently large difference in greyscale between the crystals and the glass plate for ImageJ to distinguish between crystals and background. A balance is struck between a larger field of view which allows for a greater proportion of the glass plate to be measured, versus greater magnification which allows for better imagery of the individual crystals. ImageJ's particle analysis tool was used to automate detection of the outlines of the crystals on the microscopy image and to determine the percentage of the plan view covered by the crystals. The separate drawing of the crystal outlines produced by ImageJ allows verification that the crystals have correctly been identified by the particle analysis tool (Supplemental Fig. 1). The percentage of the surface coverage is averaged for the 2-3 microscopy images.

The results from step 2 (the plate surface area in cm^2 of e.g. the low calcite-coverage area) and step 3 (the percentage of that plate area covered by calcite crystals) are combined to provide the two-dimensional (2D) surface area of calcite crystals for a given type of calcite-coverage area. To switch to a three-dimensional (3D) estimate of surface area, the 2D surface area is multiplied by five for the low calcite-coverage areas and by one for the complete calcite-coverage areas. For the low-coverage areas this assumes that, on average, the microscopy imagery displays the tops of regular six-sided rhombohedral crystals, of which five sides are available for calcite precipitation. For complete calcite-coverage areas we assume that the 3D surface area is equal to the 2D surface area. For the high calcite-coverage areas we multiply the 2D surface area by five or three: five where there is no or little overlap between adjacent crystals, three when there is sufficient overlap between adjacent crystals to require reducing the 3D surface area in this way. We do not establish or apply surface roughness to these surface areas and therefore the estimates obtained are minimum surface areas for which uncertainties are difficult to assess.

Using eight experiments (growth amounts 0.06 mmol, 0.15 mmol, 0.3 mmol, 0.5 mmol, 0.7 mmol, 2.3 mmol, 7.2 mmol and 8.3 mmol), we calculate the relationship between surface area and growth mass. Crystal surface

area for each experiment was defined using a collection of at least nine sub-images of the plate, to account for factors such as heterogeneous crystal coverage. Surface area (SA) increases logarithmically with respect to calcite growth and can be fitted with equation 1 (Supplemental Fig. 2).

$$\mathrm{SA} = 12.2(\pm 0.5) \times \ln(\mathrm{x}) + 41.0(\pm 0.7) \tag{1}$$

In equation 1, x denotes calcite growth amount (mmol).

Surface area normalised growth (SA normalized growth) is the growth amount divided by surface area, equation 2:

$$\text{SA normalized growth} = \frac{\mathrm{x}}{12.2 \times \ln(\mathrm{x}) + 41.0} \tag{2}$$

Assuming a constant non-normalised growth rate k ($\mathrm{mmol\,s^{-1}}$), equation 2 can be re-written as a function of time (t, in seconds), as per equation 3:

$$\text{SA normalized growth} = \frac{\mathrm{k} \times t}{12.2 \times \ln(\mathrm{k} \times t) + 41.0} \tag{3}$$

The surface area normalised growth rate is then the derivative of equation 3 with respect to time, simplified in equation 4:

$$\text{SA normalized growth rate} = \mathrm{k}\left(\frac{\mathrm{SA} - 12.2}{\mathrm{SA}^2}\right) \tag{4}$$

For any measured growth mass, the surface area normalised growth rate is then calculated using the total growth amount, x, and duration, t, of the experiment. Uncertainty on the surface area normalized growth rate is assessed using a Monte Carlo simulation, accounting for uncertainty of the logarithmic best fit between surface area and growth mass (equation 1).

2.7. pH and DIC concentration applicable to calcite growth

Our $CaCO_3$ samples measured for δ^7Li are recovered from the side of the 'splash zone' (blue dashed rectangle, Fig. 6A). The glass plate is resupplied with a $\sim$0.14 mL drop of fresh, unevolved solution (from a separate carboy sealed specifically against CO_2(g) loss) every $\sim$ 10 seconds on average. This fast drip rate

and the constant solution replacement ensures constant growth conditions throughout the 21 day experiment duration. Growth on our plate is nevertheless from a thin-film solution, known to outgas excess CO_2 rapidly, which constitutes our deliberate cave-analogue calcite-precipitation mechanism. Here we take account of the rapid rate of CO_2 degassing (complete within a maximum of $\sim$ 13 seconds) to calculate pH_t and $[DIC]_t$ applicable to our calcite growth. The rates of CO_2 degassing specific to these thin films, the response rate of pH to this degassing and the rate of subsequent calcite precipitation are known from existing studies including Usdowski (1982); Zeebe et al. (1999); Dreybrodt and Scholz (2011); Dreybrodt (2012). We use the CO_2 degassing (τ_{out}), pH equilibration (τ_{eq}), and calcite precipitation (τ_{pr}) time constants from Dreybrodt and Scholz (2011); Dreybrodt (2012) to establish $[DIC]_t$ and pH_t applicable to our $\delta^7Li_{calcite}$. At 15 °C, $\tau_{out} = 2.6$, $\tau_{eq} = 78$, $\tau_{pr} = 500$ seconds respectively, with 95% of degassing, pH equilibration and calcite precipitation within 3τ, i.e. within 8, 234 and 1500 seconds respectively. Because each subsequent step is longer by about an order of magnitude, the steps are regarded as subsequent in time, a reasonable approximation to reality. The drips supplying solution to the plate form within an upturned pipette tip, analogous to a cave soda straw, from which it has been shown that negligible CO_2 degassing and pH evolution occurs (Dreybrodt, 2012). Consequently we only consider solution evolution during residence time on the glass plate. Directly under the falling drip the solution residence time is $\sim$ 10 seconds. At the further reaches of our sampling area, the residence time will be longer (micro-droplets reaching these more distant areas are smaller and take longer to fully replace the existing solution), which explains the increased growth mass further from the drip impact point (c.f. Dreybrodt, 2012 and Day and Henderson, 2012 for a more in-depth discussion). For the sake of these pH_t and $[DIC]_t$ calculations we estimate the average residence time of solution applicable to our $\delta^7Li_{calcite}$ measurements to be 30 seconds, with reasonable agreement between our measured growth mass values and those predicted from applying 30 seconds to the τ_{pr} precipitation rate. In all cases carbonate precipitation is slow compared with CO_2 degassing and with the subsequent pH response, therefore we ignore the small impact of carbonate precipitation on reducing $[DIC]_t$ and pH_t. This is supported by mass-balance calculations demonstrating low levels of Ca precipitation from solution applicable to the whole plate (table 3), with even lower levels of calcite precipitation within the 'splash-zone'.

At all temperatures CO_2 degassing is complete within the 30 second solution residence time. We therefore calculate $[DIC]_t$ applicable to δ^7Li_{solid} as the original starting solution $[DIC]_0$ (equilibrated with 20 000 ppmv of headspace CO_2) minus the excess CO_2 (rapidly degassed in the cave environment). These concentrations

are calculated with PHREEQC (Parkhurst and Appelo, 1999) using the same scripts used to prepare our initial solutions. The small amount of calcite precipitating within the 'splash zone' is not accounted for.

To calculate pH_t applicable to $\delta^7Li_{CaCO_3}$, we use $3 \times \tau_{out}$ to establish the time required to complete 95% of CO_2 degassing (12 seconds at 7 °C, 4 seconds at 35 °C). The remaining seconds (18 seconds at 7 °C, 26 seconds at 35 °C) are then used to establish the increase in pH_t above our measured initial solution pH_0, using τ_{eq} (147 seconds at 7 °C, 11 seconds at 35 °C) applied to $\delta pH = \Delta pH \times \exp(-t/\tau_{eq})$, where ΔpH is the difference between the equilibrated pH value (carbonate- and hydrogen-ion equilibrated) and the measured initial solution pH.

3. Results

3.1. Calcite mass, growth rate and f

Growth of solid precipitate material can be expressed in a number of ways: i) as a simple growth mass in mg, ii) as a growth rate accounting for mass and time, e.g. $\mu g\,h^{-1}$, or (iii) as a growth rate accounting for mass, time and growth surface area, e.g. $10^{-8}\,mmol\,cm^{-2}\,s^{-1}$. Wherever possible we report surface area normalised (SAN hereafter) growth rates to facilitate inter-study comparisons.

The mass of calcite growth varies from 7 mg (for the 7 °C, low-$SI_{calcite}$ experiment) to 826 mg (for the 35 °C, high-$SI_{calcite}$ experiment) over 21 days. This corresponds to growth rates ranging from $14\,\mu g\,h^{-1}$ to $1523\,\mu g\,h^{-1}$ (table 3). Modelled SAN growth rates based on the Baker et al. (1998) method range from $1.5 \times 10^{-8}\,mmol\,cm^{-2}\,s^{-1}$ to $11.3 \times 10^{-8}\,mmol\,cm^{-2}\,s^{-1}$ for our 7 °C to 25 °C cave analogue experiments (table 3). Measured cave analogue SAN growth rates range from $0.2 \times 10^{-8}\,mmol\,cm^{-2}\,s^{-1}$ to $7.5 \times 10^{-8}\,mmol\,cm^{-2}\,s^{-1}$ (table 3). The measured cave analogue SAN growth rates are consistently smaller than the modelled cave analogue SAN growth rates, particularly for the lower $SI_{calcite}$ experiments at each temperature.

At all temperatures there is a significant difference in growth rate between low- and high-$SI_{calcite}$ experiments. In units of $\mu g\,h^{-1}$ the growth rate of the high saturation index experiment is between 3 and 11× higher than that of the low saturation index experiment. For the modelled SAN growth rates, the growth rate of the high saturation index experiment is between 1.5 and 2.3× times higher than that of the low saturation index experiment.

In a separate set of 20 °C experiments investigating the effect of $[Mg]_{solution}$ on lithium incorporation, growth mass decreases with increasing $[Mg]_{solution}$. For $SI_{calcite} = 0.5$ and otherwise identical experimental conditions, growth rate decreases from $341\,\mu g\,h^{-1}$ to $75\,\mu g\,h^{-1}$ as $[Mg]_{solution}$ increases from $6.5 \times 10^{-5}\,mol\,L^{-1}$ to $4.7 \times 10^{-3}\,mol\,L^{-1}$.

The proportion of Ca remaining in solution, 'f', is close to 1 in all cases, where e.g. 0.97 signifies that 3% of the Ca in solution has precipitated from solution to form calcite. This proportion 'f' is a whole-plate average value, calculated as $1 - \frac{mol\,precipitated\,CaCO_3}{mol\,dissolved\,CaCO_3}$, with 'mol precipitated $CaCO_3$' relating to the whole plate growth, and 'mol dissolved $CaCO_3$' equal to $[Ca]_{solution}$ multiplied by the total volume of solution applied to an experiment. For all but three experiments (the 25 °C, high-$SI_{calcite}$ experiment and the two experiments at 35 °C), $f \geq 0.97$. The lowest value of f for the whole plate is $f = 0.86$ for the 35 °C, high-$SI_{calcite}$ experiment. The corresponding maximum depletion of Li in the bulk solution is 0.05%.

3.2. Microscopy and XRD crystal identification results

Microscope images (from optical and scanning electron microscopes) confirm calcite growth for all of the 7 °C, 15 °C, 25 °C and 35 °C experiments, in agreement with previous experiments following the same growth method (Day and Henderson, 2011; Reynard et al., 2011; Day and Henderson, 2013). Examples of these microscopy images are available in Fig. 2. The XRD results of experimental growth at 7 °C, 25 °C and 35 °C indicate 100% calcite in all cases. Five of the $\delta^7Li_{CaCO_3}$ measurements (identified with the '+' symbol in table 5) were carried out on aliquots of $CaCO_3$ recovered from XRD analyses that identified that material as calcite.

For the separate 20 °C study, three experiments were performed with the following Mg/Ca solution compositions: i) our standard Mg/Ca ratio of $1.9 \times 10^{-2}\,mol\,mol^{-1}$; ii) a higher Mg/Ca ratio of $1.3\,mol\,mol^{-1}$ (equivalent to Soreq cave $[Mg/Ca]_{solution}$ composition and cave temperature); and iii) Mg/Ca ratio of $3.9\,mol\,mol^{-1}$ (equivalent to 1/10 seawater [Mg] at which the Marriott et al. (2004b) experiments were conducted). The XRD results were 100% calcite for case (i), 100% high-magnesian calcite (HMC) for case (ii) and 100% aragonite for case (iii).

3.3. Li/Ca ratios and D(Li)

The $Li/Ca_{solution}$ ratio in these experiments is maintained constant at $1.4 \times 10^{-2}\,mol\,mol^{-1}$. For a given temperature there is no significant difference in D(Li) between our two growth rates (Fig. 3), where D(Li)

is defined using mole units as per section 2.5. There is a small but statistically significant decrease in D(Li) with temperature, with D(Li) = $0.0061e^{-0.015[\pm 0.008]T}$, as defined using D(Li) from the 15 °C, 25 °C and 35 °C experiments. We treat the 7 °C D(Li) results with caution because of the potential impact of seed-contributed Li, which applies only to these 7 °C experiments. Our observed decrease in D(Li) with increasing temperature agrees with Marriott et al. (2004a), although the present study has a more shallow slope (Fig. 3).

3.4. Solution pH and DIC

Measured pH_0 of the initial solutions for calcite growth, equilibrated with 20 000 ppmv CO_2(g), range between 7.1 and 7.5 (table 1). The corresponding pH_0 values for the initial solutions of the high-magnesian calcite and aragonite experiments are 7.5 and 7.7. The evolved solution pH_t, responding to in-cave CO_2 degassing, calculated for an estimated 30 second residence time of the solution, as applies to our $\delta^7Li_{CaCO_3}$ measurements, range from 7.4 to 8.1. At 7 °C there is estimated to be a maximum 0.1 pH unit increase in pH caused by CO_2 degassing applicable to $\delta^7Li_{CaCO_3}$. At 35 °C there is estimated to be up to 0.86 pH units increase in pH caused by rapid CO_2 degassing.

Calculated $[DIC]_0$ of the initial solutions equilibrated with 20 000 ppmv of headspace CO_2(g) range from 4.5×10^{-3} mol L^{-1} to 10.8×10^{-3} mol L^{-1}. Calculated $[DIC]_t$ of the on-plate growth solutions that have equilibrated with in-cave, ambient pCO_2 values range from 3.6×10^{-3} mol L^{-1} to 8.8×10^{-3} mol L^{-1}.

3.5. Lithium isotope fractionation factors

The average $1000\ln\alpha_{\text{calcite-solution}}$ (for all of our calcite experiments) is $-8.5 \pm 2(2\sigma)$.

At all temperatures, $1000\ln\alpha_{\text{calcite-solution}}$ of the two growth rate experiments are within analytical uncertainty of each other and there is no systematic pattern between low and high growth rate $1000\ln\alpha_{\text{calcite-solution}}$ (Fig. 5). There are no statistically significant Spearman correlation coefficients between $1000\ln\alpha$ and the calcite trace-element concentrations over the full range of temperature and growth rate experiments (Supplemental table 2).

There are small but statistically significant changes in $1000\ln\alpha$ with temperature and many of the solution adjustments required by the large range of temperatures investigated by our experiments (Supplemental table 1).

For the one-week, 20 °C experiments at $SI_{calcite} = 0.5$ (testing for the effect of $Mg/Ca_{solution}$), three different solid mineralogies were precipitated for the three Mg concentrations. For $Mg/Ca_{solution} = 1.9 \times 10^{-2}$ mol mol^{-1}, calcite was precipitated with $1000\ln\alpha_{calcite\text{-}solution}$ = -8.3. For $Mg/Ca_{solution} = 1.3$ mol mol^{-1}, high-magnesian calcite (HMC) was precipitated with $1000\ln\alpha_{HMC\text{-}solution}$ = -7.4. For $Mg/Ca_{solution} = 3.9$ mol mol^{-1}, aragonite was precipitated with $1000\ln\alpha_{aragonite\text{-}solution}$ = -10.7.

4. Discussion

4.1. Change in lithium fractionation factor in response to temperature, growth rate and solution composition

These experiments grow cave analogue calcium carbonates over a wide range of temperatures and over a range of growth rates at each temperature. The aim was to: i) provide $1000\ln\alpha$ and D(Li) that apply to speleothem carbonates; and ii) allow for a broad assessment of the sensitivity of $\delta^7Li_{speleothem}$ to in-cave temperature and growth rate processes (Fig. 1). Our average $1000\ln\alpha$ and associated standard deviation is $-8.5 \pm 2\,(2\sigma)$, so the in-cave variability observed so far is small compared with the $\sim$ 13‰ glacial-interglacial changes in $\delta^7Li_{speleothem}$ observed in Soreq and Tzavoa caves, attributed to glacial-interglacial changes in silicate weathering (Pogge von Strandmann et al., 2017). Although growth rate was investigated independently of other factors at each temperature, the largest change in growth rate is induced by the 28 °C increase in temperature between our 7 °C and our 35 °C experiments. This large increase in temperature also causes changes in other variables such as in the pH of the outgassing growth solution. We discuss the potential role of these variables (e.g. temperature, growth rate and pH) in controlling $1000\ln\alpha$.

4.1.1. Temperature

Despite the overall stability of our $1000\ln\alpha_{calcite\text{-}solution}$ results over a 28 °C temperature range (average $1000\ln\alpha = -8.5 \pm 2\,(2\sigma)$), we observe a statistically significant Spearman's rank correlation coefficient between $1000\ln\alpha$ and temperature at the 0.01 significance level (Supplemental table 2). We see increased fractionation between solid and solution with increasing temperature, according to the relationships $1000\ln\alpha = 1.2\,(\pm0.2)\,\frac{10^6}{T^2} - 22.4\,(\pm2.6)$ for T in Kelvin, and $1000\ln\alpha = -0.09\,(\pm0.02)T - 6.2\,(\pm0.3)$ for T in degrees Celsius. Correlation does not imply causation and we note that other variables such as growth rate, pH and $[Mg]_{solution}$ also have significant correlations with $1000\ln\alpha$, as discussed further in sections 4.1.2 and 4.1.3.

Our observed direction of change with temperature is unexpected for mass-dependent fractionation, for which we might expect decreased fractionation between solid and solution with increasing temperature, as observed e.g. for Li isotopes in clay minerals and higher temperature silicate growth reactions by Marschall et al. (2007).

Conclusions from multiple other studies, over a range of temperatures comparable to our own, suggest that temperature in unlikely to cause a significant shift in $1000\ln\alpha$ over our 28 °C range of temperatures. No relationship between temperature and δ^7Li has been found in synthetic calcite by Marriott et al. (2004a) or in corals by Hall et al. (2005). Foraminifera studies by Rollion-Bard et al. (2009), Vigier et al. (2015) and Roberts et al. (2018) observe no or minimal temperature effect on $1000\ln\alpha$. Bivalves grown at various temperatures suggest that temperature has only a minor influence on the fractionation of Li isotopes during their shell precipitation (Dellinger et al., 2018).

4.1.2. Growth rate

At each of our experimental temperatures (7 °C, 15 °C, 25 °C and 35 °C), the high $SI_{calcite}$ experiments have growth rates that are ∼1.5× higher than the corresponding low $SI_{calcite}$ experiments. These relatively small changes in growth rate have no significant impact on either D(Li) (figure 3A) or on $1000\ln\alpha$ (figure 5A). With more significant changes in growth rate, by considering combined increases in both $SI_{calcite}$ and temperature, $1000\ln\alpha$ decreases with increasing growth rate (figure 5B). As per section 4.1.1, temperature alone is not expected to impact on $1000\ln\alpha$. The linear relationship between $1000\ln\alpha$ and growth rate from the present study, $1000ln\alpha = -0.13(\pm0.04) \times GR - 7.1(\pm0.3)$, has a significant Spearman's rank coefficient at the $\rho = 0.018$ level, with uncertainties quoted as 2σ. Increased growth rates may therefore be reducing $1000\ln\alpha$, just as increased growth rate is suggested to shift D(Li) towards values that are closer to unity (Füger et al., 2019). Using a comparable selection of experiments at 25 °C and $7.5 \leq \text{pH} \leq 8.1$ we are able to reconcile D(Li) between Füger et al. (2019) and the present study using the relationship $\text{LogDLi} = 0.09(\pm0.04) \times \text{GrowthRate}(10^{-8}\,\text{mmol}\,\text{cm}^{-2}\,\text{s}^{-1}) - 3.2(\pm0.2)$. This relationship between growth rate and D(Li) is similar to the one previously defined by Füger et al. (2019), over a smaller range of growth rates, and is consistent with increasing traces/impurities becoming trapped at faster growing surfaces (e.g. Lorens, 1981; Tesoriero and Pankow, 1996; Füger et al., 2019). Our decreasing $1000\ln\alpha$ with increasing growth rate is consistent with surface entrapment models (e.g. Watson, 2004; Icopini et al., 2004; Fantle and

DePaolo, 2007; Reynard et al., 2011; DePaolo, 2011). Surface entrapment, when lighter isotopes adsorb more readily onto minerals and can become preferentially trapped by the accreting crystal surface, has already been used to explain low $1000\ln\alpha$ for Ca isotopes in these cave analogue experiments (Reynard et al., 2011). Comparison of the Marriott et al. (2004b) and Marriott et al. (2004a) studies may also suggest that increased growth rate leads to surface entrapment of the lighter lithium isotope in calcite at higher growth rates. For the same type and mass of seed material, Marriott et al. (2004b) calcite growth occurs at a rate of $0.09\,\mathrm{g\,h^{-1}}$ with an average $1000\ln\alpha$ = -2.6, whilst Marriott et al. (2004a) calcite growth occurs at the increased rate of $0.2\,\mathrm{g\,h^{-1}}$ with a significantly lower average $1000\ln\alpha$ = -8.4. Overall therefore there is some evidence that increased growth rate may lead to increasingly low $1000\ln\alpha$ for lithium isotopes. Future experiments that focus on the impact of growth rate, independently of other variables, over a wider range of growth rates than we have managed at each temperature, would be helpful for further testing the relationship between growth rate and $1000\ln\alpha$.

Given the potential importance of growth rate in defining $1000\ln\alpha$, as outlined in the above paragraph, we discuss the degree to which our experimental growth rates are applicable to calcite growth in natural caves.

Of the multiple measures of growth rate available for our laboratory experiments (table 3), we select the modelled growth rate (derived using Baker et al., 1998) for subsequent discussion, for the following reasons. With good overall agreement between our measured growth rates ($0.2\times10^{-8}\,\mathrm{mmol\,cm^{-2}\,s^{-1}}$ to $7.5\times10^{-8}\,\mathrm{mmol\,cm^{-2}\,s^{-1}}$) and modelled growth rates ($1.5\times10^{-8}\,\mathrm{mmol\,cm^{-2}\,s^{-1}}$ to $11.3\times10^{-8}\,\mathrm{mmol\,cm^{-2}\,s^{-1}}$), both of these methods provide us with a good overall measure of growth rate. Selecting modelled rates for the subsequent discussion allows for direct comparison between growth rates from laboratory experiments and from natural caves. The lack of initial seed material in the present study is another reason for favouring modelled rates on this occasion. The present batch of experiments differs from Reynard et al. (2011); Day and Henderson (2011, 2013) by starting with no seed calcite (or with minimal seed for the 7 °C experiments), and by growing the crystals for three weeks instead of one week. This approach reduces the need for seed material and for seed corrections, but it decreases growth rates until there is sufficient sample calcite to aid with the nucleation of sample growth. This is likely to explain our lower measured growth rates compared to the modelled growth rates, particularly for the low $\mathrm{SI_{calcite}}$ experiments (figure 3B).

For active, modern speleothem growth in natural caves, $\mathrm{SI_{calcite}}$ and modelled growth rates can be assessed

from cave monitoring data. We consider both $SI_{calcite}$ and modelled growth rates from three cave monitoring studies for comparison with our cave analogue laboratory experiments. Obir, Villars and Heshang caves were selected because of their extensive cave monitoring programmes and because these sites cover a wide range of average temperatures, from 4 °C to 18 °C (table 3). At Obir cave, 5 years of continuous monitoring, for three different drip sites, reveals average $SI_{calcite}$ values between 0.4 and 0.6, and a total range between 0.15 and 0.75 (Spötl et al., 2005). At Villars cave, monitoring of four drip sites within the 1995-1996 hydrological year provides average values of $SI_{calcite}$ between 0.39 and 0.51, and a total range of values between 0.03 and 0.71 (Baker et al., 1998). At Heshang cave, the average $SI_{calcite}$ values over four years of monitoring, for drip sites HS4 and HS6, are 1.01 and 1.07, with the complete range between 0.65 and 1.25 (Ruan and Hu, 2010). Our range of experimental solution $SI_{calcite}$ values is therefore applicable for the complete range of modern growth conditions in Obir and Villars caves. Reported Heshang cave drip solution $SI_{calcite}$ are up to twice those of our highest saturation index experiments, suggesting that future cave-analogue studies could usefully further increase the maximum $SI_{calcite}$ values used in these controlled experiments.

The range of modelled growth rates applicable to calcite growth in Obir, Villars and Heshang caves (0.2×10^{-8} mmol cm^{-2} s^{-1} to 3.4×10^{-8} mmol cm^{-2} s^{-1}) compares favourably with modelled growth rates for the present study (1.5×10^{-8} mmol cm^{-2} s^{-1} to 11.3×10^{-8} mmol cm^{-2} s^{-1}), c.f. table 3. Overall, this suggests that the present study provides D(Li) and $1000\ln\alpha$ for an appropriate range of growth rates for use in speleothem studies. Use of the relationship between growth rate and $1000\ln\alpha$ from the present study ($1000ln\alpha = -0.13(\pm0.04) \times GR - 7.1(\pm0.3)$) may help to refine the selection of $1000\ln\alpha$ applicable to a particular cave study.

Stalagmite 'vertical extension' is routinely used as an indicator for growth rate in past stalagmite growth. This vertical extension is simply a measure of how quickly a stalagmite increases in height, in units of e.g. µm yr^{-1}, and can conveniently be defined using radiometric dating combined with the growth-axis distance between sample ages. Whilst this is a useful indicator, we urge caution in using 'vertical extension' as a substitute for growth rate as it has multiple controls (e.g. drip rate, cave pCO_2, continuous or interrupted solution flow) and it is not a true measure of chemical reaction rates. The vertical extension of a sample could increase fivefold, simply because solution flow is extended from one to five months per year. In this case, the rate of accretion of the crystal surface is not changing, with no corresponding impact of surface-entrapment on either D(Li) or $1000\ln\alpha$. Additional indicators of past growth rate should therefore be considered, whenever

possible. Crystallographic analysis may help to assess solution $SI_{calcite}$ applicable to past speleothem growth (Frisia, 2015), therefore providing another independent indicator of growth rate.

4.1.3. Influence of the solution composition

Whilst surface entrapment, induced by increased growth rates at our higher temperature experiments, provides a viable mechanism for explaining our variation in $1000\ln\alpha$ (section 4.1.2), we need to consider the potential impact of solution composition controls. This study uses the natural speleothem growth mechanism of CO_2 degassing to induce calcite precipitation (instead of mixing $CaCl_2$ and $NaHCO_3$ in solution). By following natural growth mechanisms and by covering a wide range of temperatures and growth rates we ensure a strong sense of $1000\ln\alpha$ applicable to caves, and of its overall sensitivity to in-cave growth rates and temperatures. In doing so however we introduce the following solution changes at increasing temperature: i) changes to the initial solution stored in our solution carboys to cater for the decreasing solubility of CO_2 with increasing temperature; and ii) faster CO_2 outgassing, and faster re-equilibration to higher pH of the growth surface solution at higher temperatures.

To cater for CO_2 solubility decreasing with temperature (whilst maintaining constant $SI_{calcite}$, X/Ca ratios, pCO_2 in the initial solution carboy, and pCO_2 in the carbonate-precipitation chamber), we adjusted solution [Ca]. The total reduction of [Ca] is from 4.8×10^{-3} (7 °C, $SI_{calcite} = 0.6$) to 2×10^{-3} mol L^{-1} (35 °C, $SI_{calcite} = 0.1$), with corresponding reductions in trace-element concentrations to maintain constant X/Ca ratios. The Spearman correlation coefficients between the non-independent changes in $1000\ln\alpha$ and solution pH_t, $[DIC]_0$, $[DIC]_t$, [Li], [Mg], [Co], [Sr] and [Ba] are all statistically significant at the 0.01 or 0.05 level (Supplemental table 1). Correlation does not require causation in all of these cases and we note that between 7 °C and 25 °C (the range of temperature for which we can produce modelled growth rates), the decrease in elemental concentrations is small (∼2.1×) in comparison with the ∼7.5× increase in growth rate. We discuss two of these variables, pH and $[Mg]_{solution}$, in more detail.

Investigations into the potential impact of pH on lithium incorporation feature in a number of studies. Füger et al. (2019) suggests influences of both growth rate and pH on D(Li), but does not report on $1000\ln\alpha$. The range of pH values applicable to these cave-analogue experiments is midway through the range of pH values investigated by Füger et al. (2019). So, whilst growth rate can reconcile these two significantly different sets of D(Li) (figure 3B,C, section 4.1.2), pH cannot. However, the small shift towards lower D(Li)

as our experiments increase in pH, temperature and growth rate would suggest that pH (in agreement with Füger et al., 2019), or temperature, rather than growth rate, is the dominant control for D(Li). For $1000\ln\alpha$ there is no significant correlation between measured pH_0 of our carboy-stored initial solution (pH 7.1 to 7.5) and $1000\ln\alpha$, but a significant correlation between pH_t and $1000\ln\alpha$ (i.e. taking account of the evolution of the growth solution chemistry during residence on the glass plate). The linear relationship is $1000\ln\alpha = -3.4(\pm0.6)pH_t + 18(\pm5)$. There is no systematic variation in pH for the experiments of Marriott et al. (2004a) or Marriott et al. (2004b). Vigier et al. (2015) observe no relationship between the pH of their solutions and δ^7Li during their laboratory culturing of foraminifera genus *Amphistegina*. They do report a positive correlation between DIC and δ^7Li of their foraminifera, although they propose a biological mechanism for this relationship. In similar culture experiments Roberts et al. (2018) do not find a significant response of *Amphistegina* to DIC, but instead observe a strong negative correlation between δ^7Li and pH. They hypothesise that it is the change in hydroxyl concentration $[OH]^-$ with pH, altering the hydration sphere of Li^+ and therefore lithium desolvation which influences the change in lithium isotopic fractionation. The linear relationship applicable to Roberts et al. (2018) is $1000\ln\alpha = -3.5pH + 26$. Whilst the present study and Roberts et al. (2018) observe the same slope (~ -3.5) between $1000\ln\alpha$ and pH (Fig. 5), there is a significant offset in the $1000\ln\alpha$ of these two studies (~ 7), which is not resolved by pH alone. Unfortunately there is no viable way of comparing the growth rates of Roberts et al. (2018) with those of the present study, to assess whether growth rate may account for the offset in $1000\ln\alpha$. Overall, over the relatively small range of pH values applicable to the present study, which is covarying with temperature and growth rate, we cannot robustly assess the impact of pH on $1000\ln\alpha$, although that would be a useful objective for future work.

For our main set of experiments, the 2.4× change in $[Mg]_{solution}$ (to account for decreased CO_2 solubility at higher temperature) is probably too small to impact on D(Li) or on $1000\ln\alpha$. For larger changes in $[Mg]_{solution}$ however, magnesium in solution is known to impact on calcite precipitation, ultimately impeding calcite precipitation sufficiently that high-magnesian calcite or aragonite is precipitated instead of calcite, as was observed during our subset of 20 °C experiments. For these 20 °C experiments, that replicate the temperature (∼20 °C) and $[Mg]_{solution}$ ($\sim 2.5 \times 10^{-3}$ mol L^{-1}) of Soreq cave, we grew high-magnesian calcite at a lower growth rate than our control 20 °C calcite experiment, with $1000\ln\alpha$ of -7.3 ± 0.6 (instead of -8.3 ± 0.5) and higher D(Li) = 1.3×10^{-2} (instead of 3.2×10^{-3}). Using $[Li]_{solution}$ and $[Li]_{calcite}$ from Pogge von Strandmann et al. (2017) and an average $[Ca]_{solution}$ from Burstyn (2019), we estimate that D(Li)

for Soreq cave ranges between 2.6×10^{-2} and 1.2×10^{-1}. It is of interest that by changing $[Mg]_{solution}$ alone ($\sim$43$\times$) our experimental D(Li) and $1000\ln\alpha$ both tend towards the higher measured values from Soreq cave.

4.2. Lithium isotopic fractionation in inorganic carbonates and biogenic carbonates of different mineralogies

Comparing our cave-analogue results with the small number of inorganic fractionation factors available in the literature, there is close agreement between aragonite experiments and measurements from aragonite grown in natural settings (despite very different growth conditions), and variable agreement between the calcite studies.

For aragonite, this study's cave-analogue $1000\ln\alpha$ ($-10.7 \pm 0.5, 2\sigma$) is within uncertainty of the Marriott et al. (2004b) aragonite samples ($-11.7 \pm 0.5, 2\sigma$), and is within uncertainty of the range (-10.5 to -7.7) of the 25 °C experimental aragonite samples of Gabitov et al. (2011), despite significant differences in the growth conditions and growth solution compositions. Our cave-analogue aragonite was grown from a freshwater, thin-film solution induced by CO_2 degassing (section 2.1), whilst the Gabitov et al. (2011) and Marriott et al. (2004b) aragonite samples were grown in artificial-seawater beaker experiments (table 4). It is encouraging that in these cases of inorganic aragonite precipitation, fractionation factors are not appearing to be sensitive to growth conditions or to solution compositions. Pure aragonite bulk carbonates from core tops sampled in the Bahamas have $\Delta^7Li_{aragonite-seawater} = -9.6 \pm 0.6‰$ that is consistent with these laboratory inorganic aragonite samples(Pogge von Strandmann et al., 2019b).

For calcite, the average $1000\ln\alpha$ from our cave-analogue experiments (-8.5) is within uncertainty of Marriott et al. (2004a) (average -8.4), but significantly different from Marriott et al. (2004b) (average -2.6). The Marriott et al. (2004a) experiments are beaker experiments, with the inclusion of Li^+, $CaCl_2$ and $NaHCO_3$ to ensure calcite precipitation with Li incorporation. The Marriott et al. (2004b) experiments have the same general setup as Marriott et al. (2004a), but with the following solution characteristics: i) Na^+, Ca^{2+}, Sr^{2+}, Cl^-, Br^-, F^- at concentrations equivalent to those in seawater, ii) Mg & U set to 1/10 of seawater concentration, iii) Li^+, U^{4+}, Cd^{2+}, Ba^{2+}, Zn^{2+} at 10$\times$ their seawater concentration, iv) sulphate was omitted to ensure calcite precipitation instead of aragonite (table 4). As per section 4.1.2, the significantly slower growth rate may help to explain the less negative $1000\ln\alpha$ of Marriott et al. (2004b) compared with $1000\ln\alpha$ of Marriott et al. (2004a), with the higher concentrations of calcite-inhibiting elements (e.g. Mg) potentially explaining the lower growth rates of Marriott et al. (2004b). However there are many differences

between those two sets of beaker experiments, which makes it difficult to fully assess the large difference in $1000\ln\alpha$ between them.

Modern-day solution and calcite measurements from Soreq cave (Pogge von Strandmann et al., 2017) provided early insight into differences between $\delta^7Li_{calcite}$ and $\delta^7Li_{solution}$ from a natural cave environment. At the modern cave temperature of 20 °C, the Soreq $\delta^7Li_{calcite}$ was lower than $\delta^7Li_{solution}$ by 3.6 and 5.2‰ from two drip sites. These Soreq cave values are quite different from our cave-analogue $1000\ln\alpha$ of −8.5. We suggest two main reasons for this: i) calcite and solution δ^7Li are not fully comparable for Soreq cave measurements unlike for laboratory experiments; ii) differences in solution chemistry between Soreq cave and our cave analogue experiments. Regarding (i), the Soreq calcite applicable to the two drip sites is from cave carbonates precipitated onto concrete paths laid in the 1970s. Measurements on modern drip waters from multiple drip sites were collected on select days in 2014 with values ranging from 20.3 to 23.9‰. A limitation, in this case, is that $\delta^7Li_{solution}$ represents a short moment in time (a few days in 2014), whereas the measured carbonates integrate decades worth of carbonate precipitation since 1970, over which time $\delta^7Li_{solution}$ may have been impacted by anthropogenic inputs (Pogge von Strandmann et al., 2017). Regarding (ii), Soreq cave is overlain by dolomitic limestone. Compared with the present study, the major solutions differences are that Soreq cave has significantly higher [Mg], [Sr], [Ba] ($\sim 43\times$, $7\times$, $6\times$ higher respectively, Burstyn, 2019), significantly lower [Li] ($\sim 280\times$, $[Li]_{solution} \sim 1.5 \times 10^{-7}\,mol\,L^{-1}$, Pogge von Strandmann et al., 2017) and includes $\sim 2 \times 10^{-3}\,mol\,L^{-1}$ of sulphate. Mg in solution is known to impact the rates and mineralogy of carbonate precipitation, due to adsorption of Mg on the growth surface, which can destabilise and enhance the solubility of the carbonate precipitate (e.g. Berner, 1975). As was discussed in greater detail in the section on solution controls (4.1.3), it is of interest that, as we replicate the $\sim 43\times$ higher $[Mg]_{solution}$ concentrations of Soreq cave, we observe a shift towards the higher partition coefficient and the higher lithium isotopic values that may apply to Soreq cave. Other caves located within dolomitic bedrock may also need to account for the impact of significantly higher $[Mg]_{solution}$.

From the data compilation in Fig. 4 the differences in $1000\ln\alpha$ between carbonate mineralogies appear to be smaller than was originally suggested by the results of Marriott et al. (2004b), which reported average calcite $1000\ln\alpha$ as −2.6 and average aragonite $1000\ln\alpha$ as −11.7. Instead, all three of the mineralogies grown within the present study (at 20 °C) have fractionation factors that vary between only −7.3 and −10.7 (Fig. 4, table 5). Other results from bulk carbonates (Pogge von Strandmann et al., 2019b), benthic foraminifera

(Marriott et al., 2004b) and brachiopods (Dellinger et al., 2018) also suggest that $\delta^7Li_{calcite}$ will not always be as isotopically heavy as suggested by Marriott et al. (2004b). A smaller difference between fractionation factors applicable to calcite and aragonite is relevant for the use of bulk carbonates as recorders of past seawater lithium isotopic composition. Whilst $\delta^7Li_{\text{bulk carbonate}}$ from a single carbonate mineralogy will always be preferable, smaller differences in $1000\ln\alpha$ between mineralogies means that a small contribution of e.g. calcite to a predominantly aragonite $\delta^7Li_{\text{bulk carbonate}}$ value, would have a smaller impact on the overall result. Given the significant impact of vital effects on $\delta^7Li_{foraminifera}$, this could help to reinforce the contribution of carefully selected and assessed $\delta^7Li_{\text{bulk carbonate}}$ for reconstructing past seawater δ^7Li. Based on the current agreement with our inorganic $1000\ln\alpha$, echinoderms may also constitute a favourable archive of past seawater δ^7Li.

5. Conclusions

Cave analogue experiments, conducted over a wide range of temperatures (7 °C to 35 °C), provide an average $1000\ln\alpha_{\text{calcite-solution}} = -8.5 \pm 2(2\sigma)$. This low variability in response to in-cave growth conditions is encouraging for studies seeking to use speleothem archives to reconstruct changes in weathering intensity. At each temperature, growth rate was varied, independently of other variables, by setting $SI_{calcite}$ between 0.1 and 0.6, in agreement with the type of modern growth conditions in Obir and Villars caves. This range of growth rates was too small to significantly impact on D(Li) or $1000\ln\alpha$. For the full range of experiments (with increasing temperature, growth rate, pH) we do not expect temperature to explain a small but significant decrease in $1000\ln\alpha$, in agreement with previous studies. Although results suggest that larger increases in growth rate may be shifting D(Li) closer to unity and $1000\ln\alpha_{\text{solid-solution}}$ towards lower values. Lithium partition coefficients from the present study and from Füger et al. (2019), with large inter-study differences in growth rate, fit the relationship $\text{LogDLi} = 0.09(\pm0.04) \times \text{GrowthRate}(10^{-8}\,\text{mmol}\,\text{cm}^{-2}\,\text{s}^{-1}) - 3.2(\pm0.2)$, similar to the one previously defined by Füger et al. (2019) over a smaller range of growth rates. Over our full range of cave analogue growth rates (induced by changes in both $SI_{calcite}$ and temperature) the relationship $1000\ln\alpha = -0.13(\pm0.04) \times GR - 7.1(\pm0.3)$ is significant at the $\rho = 0.018$ level. This negative relationship between growth rate and $1000\ln\alpha$ is consistent with a surface entrapment control mechanism. Factors such as growth rate and pH should be studied in greater detail, independently of other variables, to further assess their role in defining $1000\ln\alpha$. A subset of 20 °C experiments with increasing $[Mg]_{solution}$

provides $1000\ln\alpha$ and D(Li) for calcite, high-magnesian calcite (HMC) and aragonite. Our $1000\ln\alpha$ for these three mineralogies ranges between only -7.3 and -10.7. For HMC and aragonite there is close agreement with other published values of inorganic and biogenic $CaCO_3$. In agreement with measurements in bulk carbonates, some benthic foraminifera and brachiopods, this suggests that differences in $1000\ln\alpha$ between carbonate mineralogies is not always as large as the difference of 9.1 between aragonite and calcite observed by Marriott et al. (2004b).

Acknowledgements

We are grateful to Stacy Carolin for assistance, and for looking after the end of our 25 °C experiments, to Phil Holdship for trace-element measurements, to Katherine Clayton for XRD measurements, to Owen Green for assistance with microscopy, to Yuval Burstyn for sharing his Soreq cave monitoring data, to Mathieu Dellinger for sharing his compilation data used in Fig. 4. We thank Sambuddha Misra, Laurence Coogan, and three anonymous reviewers for suggestions and edits that improved this manuscript. We are very appreciative of the editorial handling and suggestions by Matthew Fantle, which contributed significantly to an improved publication. Development of Chris Day's cave-analogue setup was supported by the Natural Environment Research Council (NERC) grant NE/G003416/1, with additional support to Chris Day by the John Fell Fund (#0007911). Philip Pogge von Strandmann and Li analyses funded by the European Research Council (ERC) Consolidator grant 682760 CONTROLPASTCO2.

Bibliography

Affek, H. P., Bar-Matthews, M., Ayalon, A., Matthews, A., Eiler, J. M., nov 2008. Glacial/interglacial temperature variations in Soreq cave speleothems as recorded by 'clumped isotope' thermometry. Geochimica et Cosmochimica Acta 72 (22), 5351–5360.

Archer, D., Winguth, A., Lea, D., Mahowald, N., 2000. What caused the glacial/interglacial atmospheric pCO2 cycles? Reviews of Geophysics 38 (1999), 159–189.

Bailey, I., Hole, G. M., Foster, G. L., Wilson, P. A., Storey, C. D., Trueman, C. N., Raymo, M. E., sep 2013. An alternative suggestion for the Pliocene onset of major northern hemisphere glaciation based on

636 the geochemical provenance of North Atlantic Ocean ice-rafted debris. Quaternary Science Reviews 75,
637 181–194.

638 Baker, A., Genty, D., Dreybrodt, W., Barnes, W. L., Mockler, N. J., Grapes, J., feb 1998. Testing Theoreti-
639 cally Predicted Stalagmite Growth Rate with Recent Annually Laminated Samples: Implications for Past
640 Stalagmite Deposition. Geochimica et Cosmochimica Acta 62 (3), 393–404.

641 Bayon, G., Burton, K. W., Soulet, G., Vigier, N., Dennielou, B., Etoubleau, J., Ponzevera, E., German,
642 C. R., Nesbitt, R. W., jan 2009. Hf and Nd isotopes in marine sediments: Constraints on global silicate
643 weathering. Earth and Planetary Science Letters 277 (3-4), 318–326.

644 Berner, R. A., apr 1975. The role of magnesium in the crystal growth of calcite and aragonite from sea water.
645 Geochimica et Cosmochimica Acta 39 (4), 489–504.

646 Berner, R. A., Lasaga, A. C., Garrels, R. M., sep 1983. The carbonate-silicate geochemical cycle and its
647 effect on atmospheric carbon dioxide over the past 100 million years. American Journal of Science 283 (7),
648 641–683.

649 Bruland, K. W., Coale, K. H., Mart, L., dec 1985. Analysis of seawater for dissolved cadmium, copper and
650 lead: An intercomparison of voltammetric and atomic absorption methods. Marine Chemistry 17 (4),
651 285–300.

652 Burstyn, Y., 2019. Sub-annual Isotope and Trace Element Systematics in Water-Limited Karst Environments:
653 Implications for High-Resolution Paleoclimate Reconstructions in the Soreq Cave, Israel. Phd, The Hebrew
654 University of Jerusalem.

655 Carolin, S. A., Cobb, K. M., Adkins, J. F., Clark, B., Conroy, J. L., Lejau, S., Malang, J., Tuen, A. A., jun
656 2013. Varied response of western Pacific hydrology to climate forcings over the last glacial period. Science
657 340 (6140), 1564–1566.

658 Crocket, K. C., Foster, G. L., Vance, D., Richards, D. A., Tranter, M., dec 2013. A Pb isotope tracer of
659 ocean-ice sheet interaction: The record from the NE Atlantic during the Last Glacial/Interglacial cycle.
660 Quaternary Science Reviews 82, 133–144.

661 Day, C. C., Henderson, G. M., jul 2011. Oxygen isotopes in calcite grown under cave-analogue conditions.
662 Geochimica et Cosmochimica Acta 75 (14), 3956–3972.

663 Day, C. C., Henderson, G. M., may 2012. Response to comment on Day and Henderson "Oxygen isotopes
664 in calcite grown under cave-analogue conditions". Geochimica et Cosmochimica Acta 85, 388–389.

665 Day, C. C., Henderson, G. M., nov 2013. Controls on trace-element partitioning in cave-analogue calcite.
666 Geochimica et Cosmochimica Acta 120, 612–627.

667 Dellinger, M., Gaillardet, J., Bouchez, J., Calmels, D., Louvat, P., Dosseto, A., Gorge, C., Alanoca, L.,
668 Maurice, L., sep 2015. Riverine Li isotope fractionation in the Amazon River basin controlled by the
669 weathering regimes. Geochimica et Cosmochimica Acta 164, 71–93.

670 Dellinger, M., West, A. J., Paris, G., Adkins, J. F., Pogge von Strandmann, P. A., Ullmann, C. V., Eagle,
671 R. A., Freitas, P., Bagard, M. L., Ries, J. B., Corsetti, F. A., Perez-Huerta, A., Kampf, A. R., sep
672 2018. The Li isotope composition of marine biogenic carbonates: Patterns and mechanisms. Geochimica
673 et Cosmochimica Acta 236, 315–335.

674 DePaolo, D. J., feb 2011. Surface kinetic model for isotopic and trace element fractionation during precipi-
675 tation of calcite from aqueous solutions. Geochimica et Cosmochimica Acta 75 (4), 1039–1056.

676 Dorale, J. A., 1998. Climate and Vegetation History of the Midcontinent from 75 to 25ka: A Speleothem
677 Record from Crevice Cave, Missouri, USA. Science 282 (5395), 1871–1874.

678 Dreybrodt, W., may 2012. Comment on "Oxygen isotopes in calcite grown under cave-analogue conditions"
679 by C.C. Day and G.M. Henderson. Geochimica et Cosmochimica Acta 85, 383–387.

680 Dreybrodt, W., Scholz, D., feb 2011. Climatic dependence of stable carbon and oxygen isotope signals
681 recorded in speleothems: From soil water to speleothem calcite. Geochimica et Cosmochimica Acta 75 (3),
682 734–752.

683 Fairchild, I. J., Borsato, A., Tooth, A. F., Frisia, S., Hawkesworth, C. J., Huang, Y., McDermott, F., Spiro,
684 B., may 2000. Controls on trace element (Sr–Mg) compositions of carbonate cave waters: implications for
685 speleothem climatic records. Chemical Geology 166 (3-4), 255–269.

Fantle, M. S., DePaolo, D. J., may 2007. Ca isotopes in carbonate sediment and pore fluid from ODP Site 807A: The Ca2+(aq)-calcite equilibrium fractionation factor and calcite recrystallization rates in Pleistocene sediments. Geochimica et Cosmochimica Acta 71 (10), 2524–2546.

Foster, G. L., Vance, D., 2006. Negligible glacial-interglacial variation in continental chemical weathering rates. Nature 444 (7121), 918–921.

Frisia, S., jan 2015. Microstratigraphic logging of calcite fabrics in speleothems as tool for palaeoclimate studies. International Journal of Speleology 44 (1), 1–16.

Füger, A., Konrad, F., Leis, A., Dietzel, M., Mavromatis, V., mar 2019. Effect of growth rate and pH on lithium incorporation in calcite. Geochimica et Cosmochimica Acta 248, 14–24.

Gabitov, R. I., Schmitt, A. K., Rosner, M., McKeegan, K. D., Gaetani, G. A., Cohen, A. L., Watson, E. B., Harrison, T. M., mar 2011. In situ δ^7Li, Li/Ca, and Mg/Ca analyses of synthetic aragonites. Geochemistry, Geophysics, Geosystems 12 (3).

Genty, D., Blamart, D., Ouahdi, R., Gilmour, M., Baker, A., Jouzel, J., Van-Exter, S., feb 2003. Precise dating of Dansgaard-Oeschger climate oscillations in western Europe from stalagmite data. Nature 421 (6925), 833–837.

Gou, L. F., Jin, Z. D., He, M. Y., 2017. Using lithium isotopes traces continental weathering: Progresses and challenges. Journal of Earth Environment 8 (2), 89–102.

Hall, J. M., Chan, L.-H., McDonough, W. F., Turekian, K. K., jun 2005. Determination of the lithium isotopic composition of planktic foraminifera and its application as a paleo-seawater proxy. Marine Geology 217 (3-4), 255–265.

Hathorne, E. C., James, R. H., jun 2006. Temporal record of lithium in seawater: A tracer for silicate weathering? Earth and Planetary Science Letters 246 (3-4), 393–406.

Hendy, C. H., aug 1971. The isotopic geochemistry of speleothems-I. The calculation of the effects of different modes of formation on the isotopic composition of speleothems and their applicability as palaeoclimatic indicators. Geochimica et Cosmochimica Acta 35 (8), 801–824.

711 Hu, C., Henderson, G. M., Huang, J., Xie, S., Sun, Y., Johnson, K. R., feb 2008. Quantification of Holocene
712 Asian monsoon rainfall from spatially separated cave records. Earth and Planetary Science Letters 266 (3-
713 4), 221–232.

714 Huh, Y., Chan, L. H., Zhang, L., Edmond, J. M., jun 1998. Lithium and its isotopes in major world rivers:
715 implications for weathering and the oceanic budget. Geochimica et Cosmochimica Acta 62 (12), 2039–2051.

716 Icopini, G. A., Anbar, A. D., Ruebush, S. S., Tien, M., Brantley, S. L., 2004. Iron isotope fractionation
717 during microbial reduction of iron: The importance of adsorption. Geology 32 (3), 205–208.

718 Jacquet, S. H. M., Dehairs, F., Rintoul, S., 2004. A high resolution transect of dissolved barium in the
719 Southern Ocean. Geophysical Research Letters 31 (14), L14301.

720 James, R. H., Palmer, M. R., 2000. The lithium isotope composition of international rock standards. Chemical
721 Geology 166 (3-4), 319–326.

722 Jeffcoate, A. B., Elliott, T., Thomas, A., Bouman, C., may 2004. Precise/ Small Sample Size Determinations
723 of Lithium Isotopic Compositions of Geological Reference Materials and Modern Seawater by MC-ICP-MS.
724 Geostandards and Geoanalytical Research 28 (1), 161–172.

725 Kester, D. R., Duedall, I. W., Connors, D. N., Pytkowicz, R. M., apr 1967. Preparation of artificial seawater.
726 Limnology and Oceanography 12 (1), 176–179.

727 Kisakurek, B., James, R. H., Harris, N. B. W., Kisakurek, B., James, R. H., Harris, N. B. W., sep 2005.
728 Li and δ^7Li in Himalayan rivers: Proxies for silicate weathering? Earth and Planetary Science Letters
729 237 (3-4), 387–401.

730 Kluge, T., John, C. M., Jourdan, A. L., Davis, S., Crawshaw, J., 2015. Laboratory calibration of the
731 calcium carbonate clumped isotope thermometer in the 25 °C to 250 °C temperature range. Geochimica
732 et Cosmochimica Acta 157, 213–227.

733 Krüger, Y., Marti, D., Staub, R. H., Fleitmann, D., Frenz, M., 2011. Liquid-vapour homogenisation of fluid
734 inclusions in stalagmites: Evaluation of a new thermometer for palaeoclimate research. Chemical Geology
735 289 (1-2), 39–47.

Ku, T.-L., Knauss, K. G., Mathieu, G. G., nov 1977. Uranium in open ocean: concentration and isotopic composition. Deep Sea Research 24 (11), 1005–1017.

Liu, X.-M., Rudnick, R. L., McDonough, W. F., Cummings, M. L., aug 2013. Influence of chemical weathering on the composition of the continental crust: Insights from Li and Nd isotopes in bauxite profiles developed on Columbia River Basalts. Geochimica et Cosmochimica Acta 115, 73–91.

Lorens, R. B., apr 1981. Sr, Cd, Mn and Co distribution coefficients in calcite as a function of calcite precipitation rate. Geochimica et Cosmochimica Acta 45 (4), 553–561.

Marriott, C. S., Henderson, G. M., Belshaw, N. S., Tudhope, A. W., may 2004a. Temperature dependence of δ^7Li, δ^{44}Ca and Li/Ca during growth of calcium carbonate. Earth and Planetary Science Letters 222 (2), 615–624.

Marriott, C. S., Henderson, G. M., Crompton, R., Staubwasser, M., Shaw, S., 2004b. Effect of mineralogy, salinity, and temperature on Li/Ca and Li isotope composition of calcium carbonate. Chemical Geology 212 (1-2), 5–15.

Marschall, H. R., Pogge von Strandmann, P. A., Seitz, H.-M., Elliott, T., Niu, Y., oct 2007. The lithium isotopic composition of orogenic eclogites and deep subducted slabs. Earth and Planetary Science Letters 262 (3-4), 563–580.

Martin, J. M., Meybeck, M., mar 1979. Elemental mass-balance of material carried by major world rivers. Marine Chemistry 7 (3), 173–206.

Mattey, D., Lowry, D., Duffet, J., Fisher, R., Hodge, E., Frisia, S., 2008. A 53 year seasonally resolved oxygen and carbon isotope record from a modern Gibraltar speleothem: Reconstructed drip water and relationship to local precipitation. Earth and Planetary Science Letters 269 (1-2), 80–95.

McIntire, W., dec 1963. Trace element partition coefficients-a review of theory and applications to geology. Geochimica et Cosmochimica Acta 27 (12), 1209–1264.

Millot, R., Vigier, N., Gaillardet, J., jul 2010. Behaviour of lithium and its isotopes during weathering in the Mackenzie Basin, Canada. Geochimica et Cosmochimica Acta 74 (14), 3897–3912.

Misra, S., Froelich, P. N., 2009. Measurement of lithium isotope ratios by quadrupole-ICP-MS: application to seawater and natural carbonates. Journal of Analytical Atomic Spectrometry 24 (11), 1524.

Misra, S., Froelich, P. N., feb 2012. Lithium isotope history of Cenozoic seawater: changes in silicate weathering and reverse weathering. Science 335 (6070), 818–23.

Mokadem, F., Parkinson, I. J., Hathorne, E. C., Anand, P., Allen, J. T., Burton, K. W., 2015. High-precision radiogenic strontium isotope measurements of the modern and glacial ocean: Limits on glacial-interglacial variations in continental weathering. Earth and Planetary Science Letters 415, 111–120.

Morozov, N., 1968. Geochemistry of rare alkaline elements in oceans and seas. Oceanology 8, 169–178.

Owen, R. A., Day, C. C., Hu, C.-Y., Liu, Y.-H., Pointing, M. D., Blättler, C. L., Henderson, G. M., jun 2016. Calcium isotopes in caves as a proxy for aridity: Modern calibration and application to the 8.2 kyr event. Earth and Planetary Science Letters 443, 129–138.

Parkhurst, D. L., Appelo, C. A. J., 1999. User's guide to PHREEQC (Version 2)-A computer program for speciation, batch-reaction, one-dimensional transport, and inverse geochemical calculations. Water-Resources Investigations Report 99 (4259).

Phan, T. T., Capo, R. C., Stewart, B. W., Macpherson, G. L., Rowan, E. L., Hammack, R. W., jan 2016. Factors controlling Li concentration and isotopic composition in formation waters and host rocks of Marcellus Shale, Appalachian Basin. Chemical Geology 420, 162–179.

Pogge von Strandmann, P. A., Elliott, T., Marschall, H. R., Coath, C., Lai, Y.-J., Jeffcoate, A. B., Ionov, D. A., sep 2011. Variations of Li and Mg isotope ratios in bulk chondrites and mantle xenoliths. Geochimica et Cosmochimica Acta 75 (18), 5247–5268.

Pogge von Strandmann, P. A., Fraser, W. T., Hammond, S. J., Tarbuck, G., Wood, I. G., Oelkers, E. H., Murphy, M. J., jul 2019a. Experimental determination of Li isotope behaviour during basalt weathering. Chemical Geology 517, 34–43.

Pogge von Strandmann, P. A., Henderson, G. M., jan 2015. The Li isotope response to mountain uplift. Geology 43 (1), 67–70.

Pogge von Strandmann, P. A., Jenkyns, H. C., Woodfine, R. G., aug 2013. Lithium isotope evidence for enhanced weathering during Oceanic Anoxic Event 2. Nature Geoscience 6 (8), 668–672.

Pogge von Strandmann, P. A., Schmidt, D. N., Planavsky, N. J., Wei, G., Todd, C. L., Baumann, K.-H. H., dec 2019b. Assessing bulk carbonates as archives for seawater Li isotope ratios. Chemical Geology 530, 119338.

Pogge von Strandmann, P. A., Vaks, A., Bar-Matthews, M., Ayalon, A., Jacob, E., Henderson, G. M., 2017. Lithium isotopes in speleothems: Temperature-controlled variation in silicate weathering during glacial cycles. Earth and Planetary Science Letters 469, 64–74.

Rasband, W., 2012. ImageJ. Tech. Rept. Tech. rep., U.S. National Institutes of Health, Bethesda, Maryland, USA.

Reynard, L. M., Day, C. C., Henderson, G. M., jul 2011. Large fractionation of calcium isotopes during cave-analogue calcium carbonate growth. Geochimica et Cosmochimica Acta 75 (13), 3726–3740.

Roberts, J., Kaczmarek, K., Langer, G., Skinner, L. C., Bijma, J., Bradbury, H., Turchyn, A. V., Lamy, F., Misra, S., sep 2018. Lithium isotopic composition of benthic foraminifera: A new proxy for paleo-pH reconstruction. Geochimica et Cosmochimica Acta 236, 336–350.

Rollion-Bard, C., Vigier, N., Meibom, A., Blamart, D., Reynaud, S., Rodolfo-Metalpa, R., Martin, S., Gattuso, J.-P., aug 2009. Effect of environmental conditions and skeletal ultrastructure on the Li isotopic composition of scleractinian corals. Earth and Planetary Science Letters 286 (1-2), 63–70.

Ruan, J., Hu, C., dec 2010. Seasonal variations and environmental controls on stalagmite calcite crystal growth in Heshang Cave, central China. Chinese Science Bulletin 55 (34), 3929–3935.

Snyder, R., Bish, D., jan 1989. Quantitative analysis. In: Bish, D. (Ed.), Reviews in Mineralogy and Geochemistry. Vol. 20. De Gruyter, Ch. 5, pp. 101–144.

Spötl, C., Fairchild, I. J., Tooth, A. F., may 2005. Cave air control on dripwater geochemistry, Obir Caves (Austria): Implications for speleothem deposition in dynamically ventilated caves. Geochimica et Cosmochimica Acta 69 (10), 2451–2468.

Tesoriero, A. J., Pankow, J. F., mar 1996. Solid solution partitioning of Sr2+, Ba2+, and Cd2+ to calcite. Geochimica et Cosmochimica Acta 60 (6), 1053–1063.

Usdowski, E., 1982. Reactions and equilibria in the systems CO_2-H_2O and $CaCO_3$-CO_2-H_2O (O°C to 50°C). A review. Neues Jahrbuch fur Mineralogie, Abhandlungen.

Vervoort, J. D., Plank, T., Prytulak, J., oct 2011. The Hf-Nd isotopic composition of marine sediments. Geochimica et Cosmochimica Acta 75 (20), 5903–5926.

Vigier, N., Gislason, S. R., Burton, K. W., Millot, R., Mokadem, F., oct 2009. The relationship between riverine lithium isotope composition and silicate weathering rates in Iceland. Earth and Planetary Science Letters 287 (3-4), 434–441.

Vigier, N., Rollion-Bard, C., Levenson, Y., Erez, J., 2015. Lithium isotopes in foraminifera shells as a novel proxy for the ocean dissolved inorganic carbon (DIC). Comptes Rendus - Geoscience 347 (1), 43–51.

Von Blanckenburg, F., Bouchez, J., Ibarra, D. E., Maher, K., jul 2015. Stable runoff and weathering fluxes into the oceans over Quaternary climate cycles. Nature Geoscience 8 (7), 538–542.

Walker, J. C., Hays, P. B., Kasting, J. F., oct 1981. A negative feedback mechanism for the long-term stabilization of Earth's surface temperature. Journal of Geophysical Research 86 (C10), 9776–9782.

Watson, E., apr 2004. A conceptual model for near-surface kinetic controls on the trace-element and stable isotope composition of abiogenic calcite crystals. Geochimica et Cosmochimica Acta 68 (7), 1473–1488.

West, A., Galy, A., Bickle, M., jun 2005. Tectonic and climatic controls on silicate weathering. Earth and Planetary Science Letters 235 (1-2), 211–228.

Y Rosenthal, MP Field, R. S., Rosenthal, Y., Field, M. P., Sherrell, R. M., aug 1999. Precise determination of element/calcium ratios in calcareous samples using sector field inductively coupled plasma mass spectrometry. Analytical chemistry 71 (15), 3248–3253.

Zeebe, R. E., Wolf-Gladrow, D. A., Jansen, H., jun 1999. On the time required to establish chemical and isotopic equilibrium in the carbon dioxide system in seawater. Marine Chemistry 65 (3), 135–153.

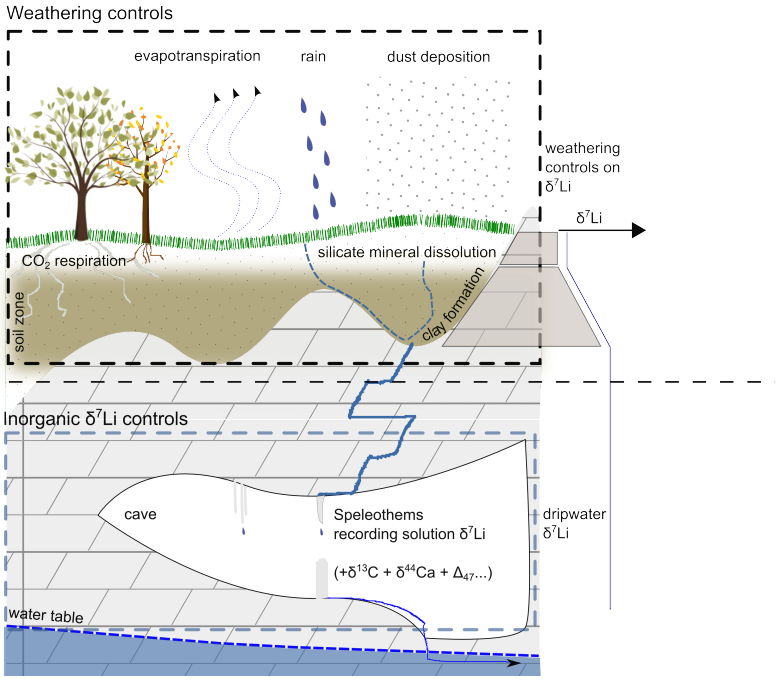

Figure 1: Cartoon illustrating the relationship between the weathering of silicates in the soil zone and the recording of this weathering activity signal in cave speleothems further down the solution flow path. An important control on $\delta^7\mathrm{Li}_{\mathrm{solution}}$, as rainwater infiltrates the soil zone, is the balance between the dissolution of silicates and the formation of clays (driving $\delta^7\mathrm{Li}_{\mathrm{solution}}$ to higher values). The depth separation between primary silicates and clay formation is somewhat idealised in this cartoon. In a karst landscape the silicates will typically be sourced from dust. The precipitation of speleothem calcite or aragonite from that infiltrating solution creates a record of $\delta^7\mathrm{Li}_{\mathrm{solution}}$ through time.

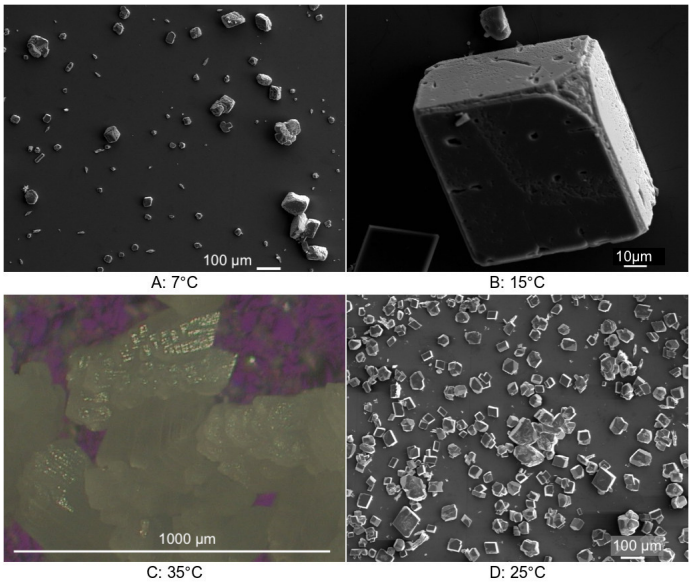

Figure 2: Selection of microscopy images (SEM and optical microscopes) of cave-analogue sample growth at different temperatures. (**A**) Sample growth at 7 °C. (**B**) Close up of 15 °C calcite growth. (**C**) Optical microscope imagery of calcite crystals at 35 °C. The frosted glass substrate is given a pink appearance by a tint plate. (**D**) Calcite growth at 25 °C.

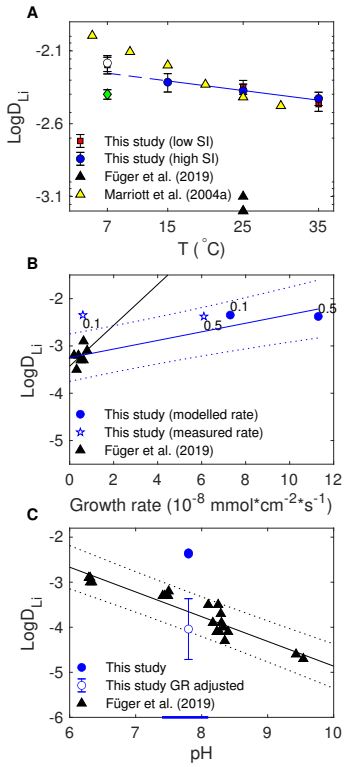

Figure 3: Lithium partition coefficients (molar ratio based in all cases). **A** $\mathrm{LogD_{Li}}$ versus temperature. Red squares (blue dots) denote the slow (fast) growth rate experiments from this study. Error bars are 2σ. The white square (white dot) is the 7 °C slow (fast) growth rate experiment from this study. The $\mathrm{LogD_{Li}}$ from these 7 °C experiments were marginally increased by seed incorporation and were used instead to correct $\delta^7\mathrm{Li_{calcite}}$ for the lithium contributed by the seed at that temperature. The green diamond is from Day and Henderson (2013). Black triangles are from Füger et al. (2019). Yellow triangles are from Marriott et al. (2004a). **B** Plot of $\mathrm{LogD_{Li}}$ versus growth rate (10^{-8} mmol cm^{-2} s^{-1}) for the 25 °C, $7.5 \leq \mathrm{pH} \leq 8.1$ experiments of Füger et al. (2019) (black triangles) and the 25 °C, $\mathrm{pH_t} = 7.8$ experiments from the present study (blue dots and blue pentagrams). Blue dots use modelled growth rates. Blue pentagrams use measured growth rates (lower than modelled rates because of an initial absence of seed material). We fit $\mathrm{LogD_{Li}} = 0.09(\pm0.04) \times \mathrm{GrowthRate}(10^{-8}\,\mathrm{mmol\,cm^{-2}\,s^{-1}}) - 3.2(\pm0.2)$ to the combined set of black triangles (Füger et al. 2019, 25 °C, $7.5 \leq \mathrm{pH} \leq 8.1$ experiments) and blue dots (this study 25 °C, $\mathrm{pH_t} = 7.8$ experiments with modelled growth rates). Uncertainty is quoted as 2σ. **C** Plot of $\mathrm{LogD_{Li}}$ versus pH for the 25 °C, $6.3 \leq \mathrm{pH} \leq 9.5$, 0.13×10^{-8} mmol cm^{-2} s^{-1} $\leq$ growth rate $\leq 0.32 \times 10^{-8}$ mmol cm^{-2} s^{-1} experiments of Füger et al. (2019) (black triangles). The black line is the unchanged relationship between $\mathrm{LogD_{Li}}$ and pH from Füger et al. (2019). Blue dots are from the 25 °C experiments of the present study (the same as in subplot B). The white dots are the blue dots with $\mathrm{LogD_{Li}}$ adjusted for the lower growth rates of Füger et al. (2019) using the relationship $\mathrm{LogD_{Li}} = 0.09(\pm0.04) \times \mathrm{GrowthRate}(10^{-8}\,\mathrm{mmol\,cm^{-2}\,s^{-1}}) - 3.2(\pm0.2)$ fitted in subplot B. The blue line on the lower pH axis highlights the range of $\mathrm{pH_t}$ for the present study.

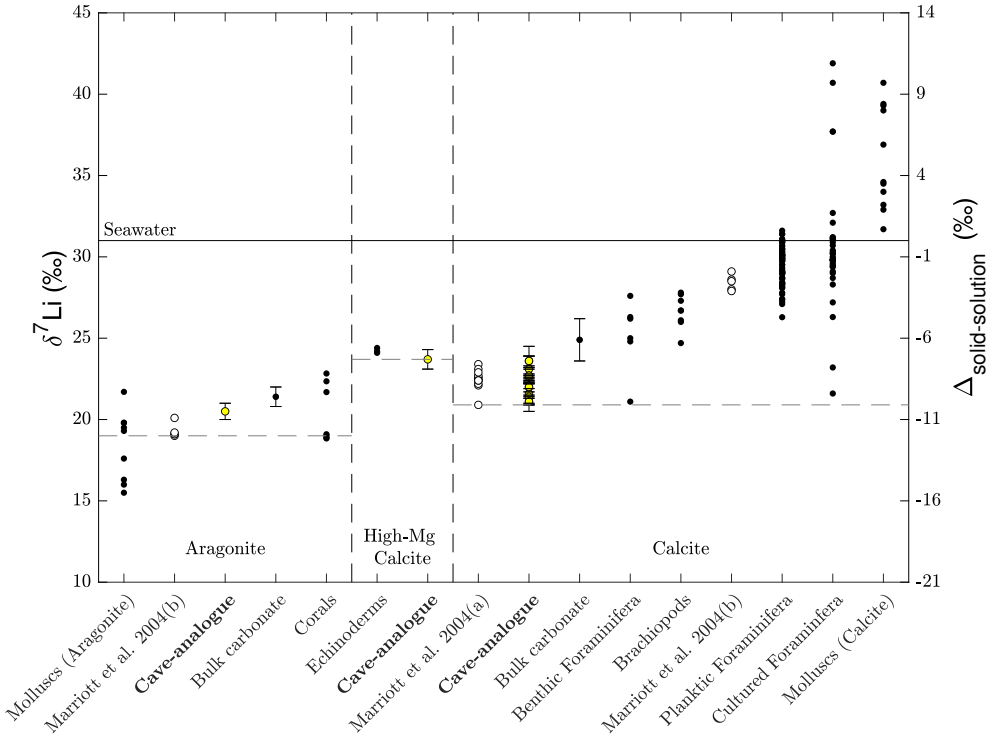

Figure 4: Compilation of δ^7Li for inorganic and biogenic $CaCO_3$, adapted from Fig. 4(A) of Dellinger et al. (2018). Laboratory experiments are denoted by white circles (Marriott et al., 2004a,b) and yellow circles (the present study). Error bars are 2σ. For these laboratory studies where $\delta^7\text{Li}_{\text{solution}} \neq \delta^7\text{Li}_{\text{seawater}}$, $\Delta_{\text{solid-solution}}$ is used to renormalise $\delta^7\text{Li}_{\text{CaCO}_3}$. Values of δ^7Li in Molluscs (aragonite), Echinoderms (high-Mg calcite), Brachiopods (calcite) and Molluscs (calcite) are from Dellinger et al. (2018), with only unmixed mineralogy cases selected. Benthic foraminifera δ^7Li are from Marriott et al. (2004b). Bulk carbonates (aragonite and calcite) are from Pogge von Strandmann et al. (2019b). Coral δ^7Li measurements are from Rollion-Bard et al. (2009) and Marriott et al. (2004b). Planktic foraminifera δ^7Li are from Hall et al. (2005), Hathorne and James (2006) and Misra and Froelich (2009). Cultured foraminifera δ^7Li are from Vigier et al. (2015). The horizontal, dashed grey lines denote the lightest inorganic $\delta^7\text{Li}_{\text{CaCO}_3}$ for each mineralogy.

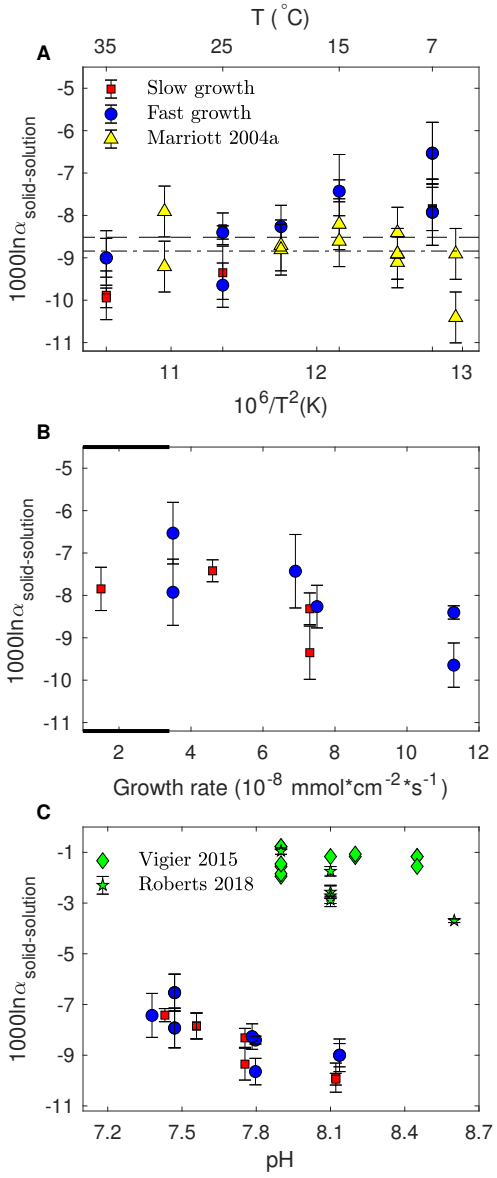

Figure 5: Plots of lithium isotopic fractionation between calcite and the growth solution. Values from this study are represented by red squares (slow growth rate experiments) and blue circles (fast growth rate experiments) in all subplots. Error bars are 2σ. Subplot **A**: $1000\ln\alpha_{\text{calcite-solution}}$ versus temperature. The dashed line represents the average value of $1000\ln\alpha$ for the cave-analogue experiments, whilst the dash-dotted line represents the average value of $1000\ln\alpha$ for the Marriott et al. (2004a) beaker experiments (yellow triangles). Subplot **B:** $1000\ln\alpha$ plotted versus growth rate, calculated using the Baker et al. (1998) model. The line of best fit is $1000ln\alpha = -0.13 \times GR(\pm 0.04) - 7.1(\pm 0.3)$, where GR is growth rate. The thicker black lines along the growth rate axes denotes the full range of modern day growth rates modelled for Heshang, Obir and Villars caves (table 3, section 4.1.2). Subplot **C**: $1000\ln\alpha$ plotted versus growth solution pH_t. The line of best fit is $1000\ln\alpha = -3.4(\pm 0.6)pH_t + 18(\pm 5)$. The green diamonds are from Vigier et al. (2015). The green pentagrams are from Roberts et al. (2018).

T	**$SI_{calcite}$**	**pH_0**	**pH_t**	**interval**	**Ca**	**Li**	**Mg**	**Co**	**Sr**	**Cd**	**Ba**
^oC				s	mol/L	mol/L	mol/L	mol/L	mol/L	mol/L	mol/L
7	0.2	7.5	7.6	10.9	$2.4x10^{-3}$	$3.8x10^{-5}$	$6.8x10^{-5}$	$1.7x10^{-9}$	$5.3x10^{-7}$	$1.2x10^{-9}$	$4.4x10^{-8}$
7	0.6	7.4	7.5	10.7	$4.8x10^{-3}$	$7.1x10^{-5}$	$1.2x10^{-4}$	$3.8x10^{-9}$	$7.6x10^{-7}$	$3.2x10^{-9}$	$6.7x10^{-8}$
15	0.2	7.2	7.4	10.7	$3.0x10^{-3}$	$3.8x10^{-5}$	$8.7x10^{-5}$	$4.9x10^{-8}$	$9.2x10^{-7}$	$4.3x10^{-8}$	$1.1x10^{-7}$
15	0.6	7.1	7.4	10.3	$4.2x10^{-3}$	$7.1x10^{-5}$	$1.4x10^{-4}$	$1.3x10^{-7}$	$1.6x10^{-6}$	$4.8x10^{-11}$	$1.7x10^{-7}$
25	0.1	7.2	7.8	10.4	$2.3x10^{-3}$	$3.0x10^{-5}$	$4.6x10^{-5}$	$7.3x10^{-10}$	$3.3x10^{-7}$	$9.0x10^{-10}$	$3.1x10^{-8}$
25	0.5	7.2	7.8	10.4	$3.3x10^{-3}$	$4.2x10^{-5}$	$6.6x10^{-5}$	$1.1x10^{-9}$	$4.7x10^{-7}$	$1.1x10^{-9}$	$4.7x10^{-8}$
35	0.1	7.3	8.1	9.5	$2.0x10^{-3}$	$2.5x10^{-5}$	$4.4x10^{-5}$	$6.2x10^{-10}$	$2.8x10^{-7}$	$5.4x10^{-10}$	$2.8x10^{-8}$
35	0.5	7.4	8.1	10.8	$2.8x10^{-3}$	$3.4x10^{-5}$	$5.7x10^{-5}$	$7.7x10^{-10}$	$3.9x10^{-7}$	$8.3x10^{-10}$	$3.9x10^{-8}$
20	0.5	7.4	7.8	10.1	$3.4x10^{-3}$	$5.0x10^{-5}$	$6.5x10^{-5}$	$4.0x10^{-9}$	$6.4x10^{-7}$	$1.8x10^{-9}$	$4.7x10^{-8}$
20	0.5	7.5	8.1	10.2	$1.9x10^{-3}$	$2.8x10^{-5}$	$2.5x10^{-3}$	$2.0x10^{-9}$	$3.4x10^{-7}$	$1.0x10^{-9}$	$3.0x10^{-8}$
20	0.5	7.7	8.3	10.2	$1.2x10^{-3}$	$1.7x10^{-5}$	$4.7x10^{-3}$	$1.3x10^{-9}$	$2.4x10^{-7}$	$7.2x10^{-10}$	$2.0x10^{-8}$
2x	RSD			10(%)	7.6(%)	8.5(%)	6.8(%)	10.7(%)	9.0(%)	43.4(%)	12.6(%)

Table 1: Starting-solution concentrations for all cave-analogue experiments in this study, based on measurements of solution aliquots from the dissolution chamber. T is temperature in degrees Celsius. $SI_{calcite}$ is the saturation index of calcite in solution. pH_0 is the measured pH of the solution in the initial solution carboy, sealed throughout the experiment with 20 000 ppmv CO_2 in the headspace. pH_t is the calculated pH value of the growth solution after thirty seconds of residing on the glass plate. The 'interval' is the time interval between two subsequent drops reaching the plate. Concentrations are in units of mol L^{-1}. The three 20 °C experiments differ based on their Mg concentration (instead of $SI_{calcite}$). The final table row is a measure of analytical uncertainty quantified using a quality control standard interspersed repeatedly during sample analysis, and expressed as 2x the relative standard deviation (RSD) on all analyses.

T	**$SI_{calcite}$**	**Li/Ca**	**Mg/Ca**	**Co/Ca**	**Sr/Ca**	**Cd/Ca**	**Ba/Ca**	**Mineralogy**
^oC		mol/mol	mol/mol	mol/mol	mol/mol	mol/mol	mol/mol	
7	0.2	$9.8x10^{-5}$	$3.1x10^{-3}$	$3.0x10^{-6}$	$2.9x10^{-5}$	$2.9x10^{-6}$	$4.5x10^{-6}$	calcite
7	0.6	$9.7x10^{-5}$	$2.6x10^{-3}$	$8.7x10^{-7}$	$3.0x10^{-5}$	$1.9x10^{-6}$	$3.4x10^{-6}$	calcite
15	0.6	$8.2x10^{-5}$	$1.5x10^{-3}$	$1.5x10^{-4}$	$4.4x10^{-5}$	$2.0x10^{-7}$	$4.1x10^{-6}$	calcite
25	0.1	$4.9x10^{-5}$	$1.3x10^{-3}$	$5.5x10^{-7}$	$1.6x10^{-5}$	$4.9x10^{-6}$	$1.7x10^{-6}$	calcite
25	0.5	$4.1x10^{-5}$	$1.0x10^{-3}$	$4.5x10^{-7}$	$1.7x10^{-5}$	$3.6x10^{-6}$	$1.7x10^{-6}$	calcite
35	0.1	$2.9x10^{-5}$	$1.1x10^{-3}$	$6.3x10^{-7}$	$1.6x10^{-5}$	$1.4x10^{-5}$	$1.4x10^{-6}$	calcite
35	0.5	$2.8x10^{-5}$	$1.1x10^{-3}$	$3.4x10^{-7}$	$1.5x10^{-5}$	$5.8x10^{-6}$	$9.7x10^{-7}$	calcite
20	0.5	$4.7x10^{-5}$	$4.8x10^{-4}$	$1.1x10^{-6}$	$1.9x10^{-5}$	$1.2x10^{-5}$	$2.2x10^{-6}$	calcite
20	0.5	$1.9x10^{-4}$	$2.8x10^{-2}$	$1.2x10^{-6}$	$3.5x10^{-5}$	$1.1x10^{-5}$	$4.4x10^{-6}$	high-Mg calcite
20	0.5	$8.3x10^{-5}$	$4.1x10^{-3}$	$7.9x10^{-7}$	$1.9x10^{-4}$	$2.2x10^{-6}$	$2.1x10^{-5}$	aragonite
2x	RSD	8.5(%)	6.8(%)	10.7(%)	9.0(%)	43.4(%)	12.6(%)	

Table 2: Solid trace-element to Ca ratios for cave-analogue experiments in this study. There was insufficient material left for the lower saturation index 15 °C experiment. T is temperature in degrees Celsius. $SI_{calcite}$ is the saturation index of calcite in solution. Cave-analogue experiments at 20 °C were conducted with three increasing values of $[Mg]_{solution}$. They are listed here in the same order of increasing [Mg] as in table 1. The final table row is a measure of analytical uncertainty quantified using a quality control standard interspersed repeatedly during sample analysis, and expressed as 2x the relative standard deviation (RSD) on all analyses.

T °C	$SI_{calcite}$	average drip interval s	growth mineralogy	f	measured growth rate $\mu g\,h^{-1}$	measured growth rate $\frac{10^{-8}\,mmol}{cm^2 s^1}$	modelled growth rate $\frac{10^{-8}\,mmol}{cm^2 s^1}$	reference
7	0.2	11	calcite	1	14		1.5	This study
7	0.6	11	calcite	1	55	0.31 ± 0.06	3.5	"
7	0.6	128	calcite	0.89	166	0.90 ± 0.09	3.5	"
15	0.2	11	calcite	0.99	99	0.52 ± 0.07	4.6	"
15	0.6	10	calcite	0.98	294	1.5 ± 0.2	6.9	"
20	0.5	10	calcite	0.98	341	1.7 ± 0.3	7.5	"
20	0.5	10	high-Mg calcite	0.97	284			"
20	0.5	10	aragonite	0.99	75			"
25	0.1	10	calcite	0.99	134	0.60 ± 0.09	7.3	"
25	0.5	10	calcite	0.89	1470	6.0 ± 0.9	11.3	"
35	0.1	10	calcite	0.94	431	1.5 ± 0.2		"
35	0.5	11	calcite	0.86	1523	5.2 ± 0.7		"
4	0.15-0.75		calcite				0.2-0.6	Obir Cave Spötl et al. (2005)
11	0.4 ± 0.3 0.5 ± 0.2 0.4 0.5 ± 0.2		calcite				2.7-3.4	Grotte de Villars Baker et al. (1998)
18	0.65-1.25		calcite				2.3-3.1	Heshang Cave Ruan and Hu (2010)

Table 3: Measured/calculated growth rates for: i) these cave-analogue experiments, and ii) a selection of natural cave studies for which there is sufficient information to establish ranges of saturation indices and modelled growth rates. Cave-analogue experiments at 20 °C were conducted with three increasing values of $[Mg]_{solution}$. They are listed here in the same order of increasing $[Mg]_{solution}$ as in table 1. Measured growth rates in units of $\mu g\,h^{-1}$ are calculated as the whole-plate growth mass divided by the duration of the experiment. Surface area normalised (SAN) growth rates in units of $10^{-8}\,mmol\,cm^{-2}\,s^{-1}$were measured with the method summarised in section 2.6. For three natural cave monitoring studies, monitored ranges of calcite saturation index values are provided: i) as the full range of published values for Obir and Heshang caves, ii) as the average and standard deviation for the monitored drip sites in the Grotte de Villars. Wherever possible we use the equations of Baker et al. (1998) to produce modelled SAN growth rates to provide some indication of the likely range in growth rates.

	This study	Marriott et al. 2004(a)	Marriott et al. 2004(b)	Füger et al. 2019	average	average
Study type	cave lab.	beaker	beaker	beaker	seawater	rivers
Mineralogy	calcite	calcite	calcite	calcite	$\mathrm{mol\,L^{-1}}$	$\mathrm{mol\,L^{-1}}$
$[Li^+]$	3.6×10^{-5}	1.8×10^{-4}	2.6×10^{-4}	3.3×10^{-4}	2.6×10^{-5}	4.3×10^{-7}
$[F^-]$			5.3×10^{-5}		5.3×10^{-5}	5.3×10^{-8}
$[Na^+]$			4.7×10^{-1}	3.0×10^{-1}	4.7×10^{-1}	2.6×10^{-4}
$[Mg^{2+}]$	5.6×10^{-5}		5.3×10^{-3}		5.3×10^{-2}	1.7×10^{-4}
$[Cl^-]$		4.2×10^{-1}	5.5×10^{-1}	3.0×10^{-1}	5.5×10^{-1}	2.2×10^{-4}
$[Ca^{2+}]$	2.8×10^{-3}	2.4×10^{-1}	1.1×10^{-2}	2.4×10^{-3}	1.1×10^{-2}	5.0×10^{-4}
$[SO_4^{2-}]$					2.8×10^{-2}	8.8×10^{-5}
$[Ba^{2+}]$	3.9×10^{-8}		7×10^{-7}		7×10^{-8}	1.5×10^{-7}
$[U^{4+}]$	3.1×10^{-10}		1.4×10^{-7}		1.4×10^{-8}	1.7×10^{-10}
Ionic Strength $(\mathrm{mol\,kg^{-1}})$	0.006 - 0.014	0.2 - 1.0	0.54	0.6	0.67	0.002
$1000 \ln \alpha$	-8.5	-8.4	-2.6			
pH	7.1 to 8.3	6.9-7.1	7.7-8.3	6.3-9.6	8.2	6.5-8.5
$CaCl_2$ input $(\mathrm{mol\,min^{-1}})$	n/a	9.4×10^{-5}	1.5×10^{-5}	1.7×10^{-7} to 6.9×10^{-7}		
$NaHCO_3$ input $(\mathrm{mol\,min^{-1}})$	n/a	1×10^{-4}	1.5×10^{-5}	1.7×10^{-7} to 6.9×10^{-7}		

Table 4: Summary of key solution characteristics for our cave-analogue experiments in comparison with the experiments of Marriott et al. (2004a,b); Füger et al. (2019), seawater and river water. All concentrations are in $\mathrm{mol\,L^{-1}}$. For the Marriott et al. (2004a,b); Füger et al. (2019) experiments, the concentrations are an average of reported concentrations, or are calculated from what the authors report having added to solution. Seawater concentrations are mostly from Kester et al. (1967), with Li seawater concentration from Morozov (1968), Cd seawater concentration from Bruland et al. (1985), Ba seawater concentration from Jacquet et al. (2004) and Uranium seawater concentration from Ku et al. (1977). River water concentrations are from Martin and Meybeck (1979).

T	$SI_{calcite}$	D(Li)	$\delta^7Li_{solution}$	δ^7Li_{CaCO3}	$1000ln\alpha_{solid\text{-}solution}$	mineralogy
7	0.2	$5.5x10^{-3} \pm 8.4x10^{-4}$	12.6 ± 0.5	4.6 ± 0.2	-7.8 ± 0.5	calcite
7	0.6	$5.5x10^{-3} \pm 8.3x10^{-4}$	12.2 ± 0.5	5.7 ± 0.5	-6.5 ± 0.7	calcite
7*+	0.6		13.4 ± 0.6	5.4 ± 0.5	-7.9 ± 0.8	calcite
15	0.2		17.1 ± 0.2	9.6 ± 0.2	-7.4 ± 0.3	calcite
15	0.6	$4.8x10^{-3} \pm 7.0x10^{-4}$	17.5 ± 0.7	10.0 ± 0.6	-7.4 ± 0.9	calcite
25	0.1	$4.5x10^{-3} \pm 4.9x10^{-4}$	12.7 ± 0.3	4.3 ± 0.2	-8.3 ± 0.4	calcite
25*+	0.1	$4.5x10^{-3} \pm 4.9x10^{-4}$	12.7 ± 0.3	3.2 ± 0.5	-9.4 ± 0.6	calcite
25	0.5	$4.2x10^{-3} \pm 4.7x10^{-4}$	13.9 ± 0.2	5.4 ± 0.0	-8.4 ± 0.2	calcite
25*+	0.5	$4.2x10^{-3} \pm 4.7x10^{-4}$	13.9 ± 0.2	4.1 ± 0.5	-9.6 ± 0.5	calcite
35	0.1	$3.4x10^{-3} \pm 3.7x10^{-4}$	12.8 ± 0.2	2.9 ± 0.5	-9.9 ± 0.6	calcite
35*+	0.1	$3.4x10^{-3} \pm 3.7x10^{-4}$	12.8 ± 0.2	2.8 ± 0.1	-9.9 ± 0.2	calcite
35	0.5	$3.7x10^{-3} \pm 3.9x10^{-4}$	13.1 ± 0.4	4.0 ± 0.5	-9.0 ± 0.6	calcite
35*+	0.5	$3.7x10^{-3} \pm 3.9x10^{-4}$	13.1 ± 0.4	4.0 ± 0.2	-9.0 ± 0.5	calcite
20*	0.5	$3.2x10^{-3} \pm 4.0x10^{-4}$	13.3 ± 0.4	4.9 ± 0.3	-8.3 ± 0.5	calcite
20*	0.5	$1.3x10^{-2} \pm 1.6x10^{-3}$	12.8 ± 0.6	5.4 ± 0.2	-7.3 ± 0.6	high-Mg calcite
20*	0.5	$5.8x10^{-3} \pm 7.1x10^{-4}$	13.1 ± 0.3	2.4 ± 0.4	-10.7 ± 0.5	aragonite

Table 5: Cave analogue D(Li) and lithium isotopic values expressed in ‰ notation relative to the LSVEC standard. The experiments marked with '*' were measured for Li isotopes at University College London instead of at the University of Oxford. The $\delta^7Li_{calcite}$ measurements marked with '+' were recovered from the XRD silicon substrates and measured for Li isotopes.

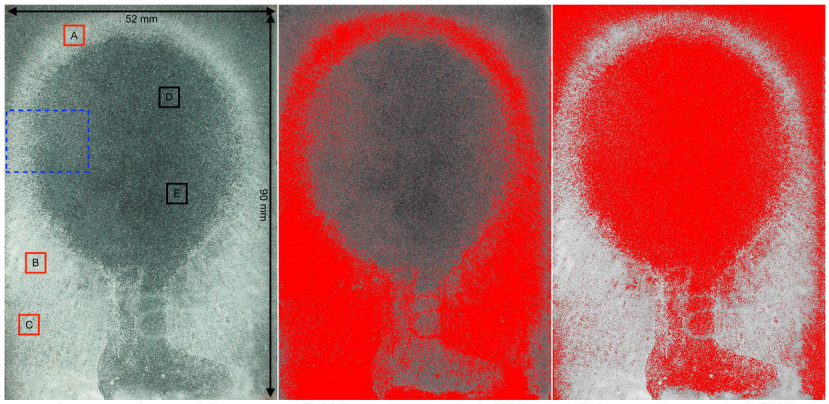

Figure 6: Three versions of the same photograph of 15 °C cave-analogue growth material, in plan view, in cross-polarised light. We use the photograph to establish the percentage of 'low' and 'high' growth areas of calcite on the plate. **A**: Whiter areas of the plate have higher amounts of calcite growth. Boxes denote areas of the plate where higher-magnification microscopy images are used for the analysis of crystal surface area (Supplemental Fig. 1). The dashed blue rectangle denotes the area where calcite was retrieved from for δ^7Li measurements. **B**: ImageJ processed image used to highlight areas of 'high-growth'. These high-growth areas (white in image A) are coloured red by the threshold function of ImageJ. ImageJ provides us with the corresponding percentage of the plate with high calcite-coverage (46%). **C**: ImageJ processed image used to highlight areas of 'low-growth'. These low-growth areas (dark in image A) are coloured red by the threshold function of ImageJ. ImageJ provides us with the corresponding percentage of the plate with low calcite-coverage (54%).